Transient response of a gyro-elastic structured medium: Unidirectional waveforms and cloaking

M. Garau[a], M.J. Nieves[a,b,*], G. Carta[c], M. Brun[b]

[a] Keele University, School of Computing and Mathematics, Keele, ST5 5BG, UK
[b] University of Cagliari, Department of Mechanical, Chemical and Material Engineering, Cagliari, 09123, Italy
[c] Liverpool John Moores University, Mechanical Engineering and Materials Research Centre, Liverpool, L3 3AF, UK

A B S T R A C T

The transient analysis of gyro-elastic structured media, composed of periodically placed masses interconnected by elastic rods and attached to gyroscopic spinners, is presented. The analysis is based on an asymptotic transient model, developed in this paper, that describes the interaction between a gyroscopic spinner and a mass embedded in a truss system. Several examples are given that illustrate the transient features of special dynamic phenomena, including unidirectional interfacial waves and highly localised waveforms. Two important applications of the model are also proposed, which demonstrate that gyro-elastic systems can be utilised to design an efficient structured topological insulator and a cloaking device for a discrete medium.

© 2019 Published by Elsevier Ltd.

1. Introduction

Gyro-elastic structured media exhibit unique dynamic properties, at both low and high frequencies, that can be used to generate special dynamic phenomena unachievable with other mechanical systems. A gyro-elastic structured medium consists of a lattice of masses, connected to each other by elastic links (such as rods or beams) and attached to gyroscopic spinners. The latter confer chirality to the lattice and can be used to break time-reversal symmetry.

The transient motion of a gyroscopic spinner is geometrically non-linear. However, if the nutation angle is small, the motion can be described by a linearised model, presented for the first time in this paper. Even within this linearised setting, masses in a gyro-elastic medium can undergo a range of atypical trajectories depending on the properties of the system. As an example, in Fig. 1 we show the motion of a gyroscopic spinner with a hinged base and a mass at its tip, which is constrained by a system of six extensional elastic springs. The results, based on a numerical scheme implemented in *Matlab*, show that the system traces a complicated trajectory. Nonetheless, the formulation presented in this paper can fully predict the transient motion of this system.

The first model of a gyro-elastic lattice was proposed in Brun, Jones, and Movchan (2012), where the time-harmonic analysis of a monatomic and bi-atomic triangular array of masses connected to gyroscopic spinners was carried out. In Carta, Brun, Movchan, Movchan, and Jones (2014), the dynamic response of this system subjected to different external excitations was investigated, with special attention given to tunable dynamically induced anisotropy occurring at specific frequencies. In particular, it was observed that in correspondence with the stationary points of the dispersion surfaces, waves
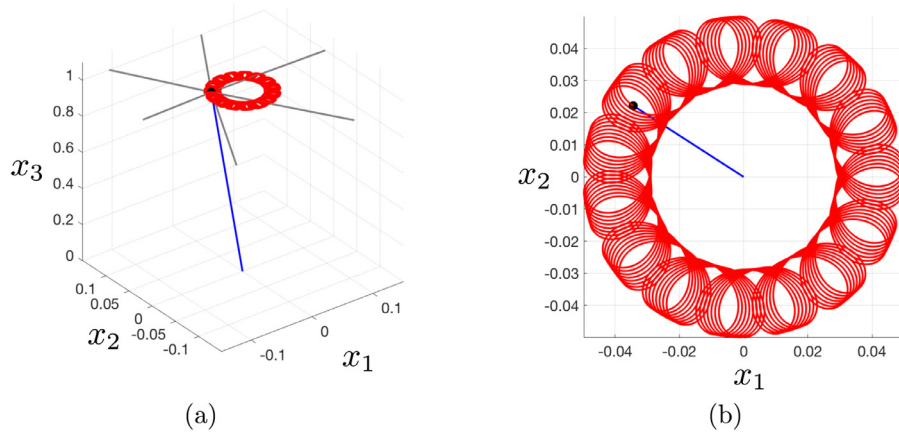

Fig. 1. The motion of a single gyroscopic spinner. The gyroscopic spinner is hinged at its base and connected to a mass m at its tip. The mass is also constrained by a system of six extensional springs. The spinner is represented by the blue line and the mass m by the black dot. The six grey lines indicate the springs attached to the mass. (a) Representation of the system with the trajectory of the mass shown in red. (b) Planar view of the system showing a magnification of the path traced by the mass. The motion of this system is illustrated in the Video 1 of the Supplementary Material. (For interpretation of the references to colour in this figure, the reader is referred to the web version of this article.)

are forced to travel along some preferential directions, depending on the orientation of the external force. Wave propagation can even be localised in a single narrow line, if two types of spinners with *ad hoc* properties are introduced into the structure, as discussed in Carta, Jones, Movchan, Movchan, and Nieves (2017a). This localised wave pattern, which resembles a Gaussian beam, can be deviated by changing the arrangement of the spinners inside the lattice. As a result, the localised wave can be forced to follow a closed path through multiple deviations, causing the wave amplitude to increase significantly. This phenomenon has been named DASER (Dynamic Amplification by Spinners in Elastic Reticulated systems). In Carta et al. (2017a), the localised wave pattern was obtained in the time-harmonic regime, while here we demonstrate that this dynamic effect can also be attained in the transient regime.

Gyroscopic spinners have been utilised to break time-reversal symmetry and create topological insulators. In Wang, Lu, and Bertoldi (2015) and Garau, Carta, Nieves, Jones, Movchan, and Movchan (2018) it was shown that hexagonal gyro-elastic structures can support edge and interfacial waves at frequencies associated with dispersion degeneracies possessed by such media. The gyroscopic spinners allow one to modify the topology of these degeneracies, also known as Dirac points. At frequencies in the vicinity of such points, waves can propagate along the boundary of the structured medium or the boundary of a sub-domain, leaving the bulk of the medium almost undisturbed. Unidirectionally propagating edge modes immune to backscattering and localisation due to geometrical and material defects were firstly observed in photonic crystals (Gao et al., 2015; He et al., 2010; Khanikaev, Mousavi, Tse, Kargarian, MacDonald, & Shvets, 2013; Raghu & Haldane, 2008; Wang, Chong, Joannopoulos, & Soljačić, 2008). In Raghu and Haldane (2008), it was shown that these modes are analogs of the edge states associated with the quantum Hall effect. The existence of unidirectional edge states in plasmons was demonstrated in Jin, Christensen, Soljačić, Fang, Lu, and Zhang (2017) at infrared frequencies. Topological acoustic insulators supporting one-way edge sound modes were proposed in Khanikaev, Fluery, Mousavi, and Alú (2015), Ni, He, Sun, Liu, Lu, and Feng (2015), Yang et al. (2015), Chen and Wu (2016), He et al. (2016), Souslov, van Zuiden, Bartolo, and Vitelli (2017) and Zhou and Zhao (2019). An elastic analog of the quantum Hall effect for plates was discussed in Pal and Ruzzene (2017). Helical edge states were experimentally observed in a lattice of mechanical oscillators in Süsstrunk and Huber (2015). Recently, one-way interfacial rotational waves were generated in a granular crystal, where the interaction between the beads is based on non-central contact forces (Zheng, Teocharis, Tournat, & Gusev, 2018). A theoretical approach based on group theory and topological concepts were used in Makwana & Craster (2018a,b) to design platonic crystals possessing topological valley supernetworks and multi-directional energy splitters.

In this paper, we demonstrate the existence of unidirectional interfacial and edge waves in a hexagonal gyro-elastic lattice. While in Garau et al. (2018) the formulation was developed in the time-harmonic regime, here the analysis of topologically protected edge modes is performed in the transient regime using the asymptotic model developed in this paper. An illustrative example is shown in Fig. 2, where we consider waves propagating in a rectangular slab of hexagonal lattice, that is partitioned into two subdomains defined by the arrangement of spinners to which the lattice is connected. The subdomains have a zig-zag type interface and the lattice is excited at a specific frequency at the location shown in the figure. A unidirectional interfacial wave propagates along the sharp bends of this internal boundary and travels along the interface to the right side of the lattice. We remark that the direction is reversible by either interchanging the properties of the spinners on either side of the interface or by adjusting the frequency of excitation. The model is detailed in Section 3.

Gyroscopic spinners have further applications in the design of elastic cloaking devices (Brun, Colquitt, Jones, Movchan, & Movchan, 2014; Brun, Guenneau, & Movchan, 2009; Colquitt, Brun, Gei, Movchan, Movchan, & Jones, 2014; Farhat, Guenneau, Enoch, & Movchan, 2009; Milton, Briane, & Willis, 2006; Norris, 2008; Norris & Shuvalov, 2011; Parnell, 2012). In
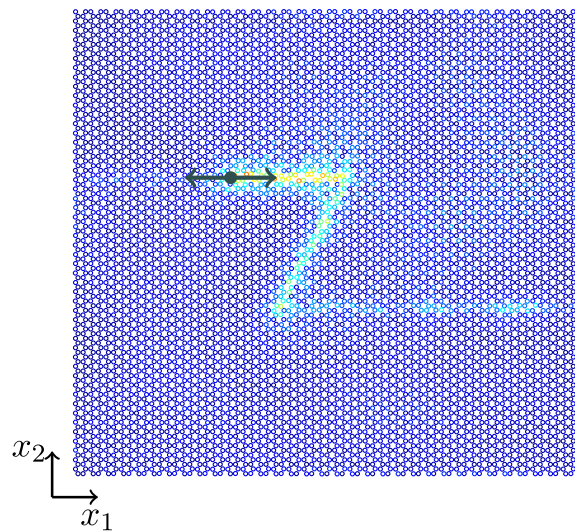
Fig. 2. Hexagonal lattice connected to an array of gyroscopic spinners. Interfacial waves are produced by a concentrated load applied at the point indicated with a black dot. Waves propagate in the transient regime following a zig-zag pattern. Technical details are reported in Section 3 and a video of the motion is included in the Supplementary Material (see Video 2). (For interpretation of the references to colour in this figure, the reader is referred to the web version of this article.)

Brun et al. (2012), the time-harmonic equations of the triangular gyro-elastic lattice were homogenised to show a possible design for an inertial micro-polar elastic continuum. The elastic metamaterial is capable of strongly reducing the scattering caused by the presence of a stiff defect in a homogeneous elastic material. In Brun et al. (2012) the effectiveness of this cloaking device was shown numerically in the time-harmonic regime. In this article, we also show that the model considered allows one to create a structured cloaking device for a hexagonal lattice and the effectiveness of this cloak is analysed in the transient regime.

Recently, a renewed interest in structural mechanics has grown from the development of new concepts in different technological fields, for example in locomotion (Bigoni, Dal Corso, Misseroni, & Bosi, 2014; Dal Corso, Misseroni, Pugno, Movchan, Movchan, & Bigoni, 2017; Rafsanjani, Zhang, Liu, Rubinstein, & Bertoldi, 2018), structural folding (Bosi, Misseroni, Dal Corso, & Bigoni, 2015), soft robotics (Armanini, Dal Corso, Misseroni, & Bigoni, 2017; Cazzolli & Dal Corso, 2019), and metamaterials (Bordiga, Cabras, Bigoni, & Piccolroaz, 2018; Cabras, Movchan & Piccolroaz, 2017; Kochmann & Bertoldi, 2017; Misseroni, Colquitt, Movchan, Movchan, & Jones, 2016; Piccolroaz, Movchan, & Cabras, 2017a; 2017b).

With respect to the analysis of gyroscopic effects in mechanics, we mention Kirillov (2013), where perturbation methods were developed to analyse the stability of multi-parameter gyroscopic systems in the presence of non-conservative forces. In addition, the Krein-space approach for tackling non-conservative gyroscopic systems was proposed in Kirillov (2009).

The notion of a gyro-elastic system introduces a potentially vast array of new pathways, not only in the construction of microstructured materials, but also in the design of larger scale structures commonly encountered in civil engineering. Innovative tunable resonator systems that utilise gyroscopic spinners can be implemented in civil engineering structures to help in inhibiting failure processes. Simplified models of dynamic failure processes in civil engineering structures have been considered in Brun, Movchan, and Slepyan (2013), Brun, Giaccu, Movchan, and Slepyan (2014), Nieves, Mishuris, and Slepyan (2016) and Nieves, Mishuris, and Slepyan (2017). In Carta, Jones, Movchan, Movchan, and Nieves (2017b) a resonator system composed of gyro-elastic beams was designed to suppress the vibrations of a long structure, such as a bridge, subjected to seismic waves. The theory of gyro-elastic beams was firstly developed in D'Eleuterio and Hughes (1984) and Hughes and D'Eleuterio (1986) and gyroscopic problems in elasticity were studied in Padovan (1978, 1979) and Padovan and Adams (1980). In practice, gyro-elastic beams can be designed and constructed by attaching gyroscopic spinners to elastic beams, as detailed in Carta, Nieves, Jones, Movchan, and Movchan (2018), and Nieves, Carta, Jones, Movchan, and Movchan (2018), and this has led to the micro-structural characterisation of a gyro-elastic beam. Functionally graded microbeams, possessing microstructure and having applications in the design of micro-electro-mechanical systems, have been considered in Ghayesh, Farokhi, and Gholipour (2017), Farokhi, Ghayesh, Gholipour, and Hussain (2017) and Ghayesh (2018, 2019). The dynamics of rotating microbeams can be found in Dehrouyeh-Semnani (2015), Dehrouyeh-Semnani, Jouybari, and Dehrouyeh (2016) and Shafiei, Kazemi, & Ghadiri (2016). Other applications of gyro-elastic continua can be found in aerospace engineering, where they allow for the control of the attitude and shape of spacecraft Hughes (1986), D'Eleuterio and Hughes (1987), Yamanaka, Heppler, & Huseyin (1996) and Hassanpour and Heppler (2016a,b). Gyroscopic coupling is also exploited to design smart structures that optimise the dissipation of vibration energy (Del Vescovo & Giorgio, 2014). For a lattice, the coupling of in-plane motions may be achieved through the tuning of its micro-structural geometry, supplying chirality to the system (Bacigalupo & Gambarotta, 2016; Lepidi & Bacigalupo, 2018).

The time-harmonic models for gyro-elastic lattices studied in Brun et al. (2012), Carta et al. (2014, 2017a) and Garau et al. (2018) show how the presence of gyroscopic spinners at the lattice junctions affects the motion of the system, allowing one to achieve a variety of special dynamic phenomena. In particular, the spinners enforce a coupling between the angular momentum balance of the gyroscopic spinners and the linear momentum balance of the lattice particles. The transient analysis developed here allows us to fully describe various wave propagation phenomena, such as unidirectional waves. Within the scope of possible technological applications, the transient regime enables us to completely determine the performance of the new generation of structured elastic metamaterials.

The paper is organised as follows. In Section 2, we develop the formulation for the transient motion of a gyroscopic spinner connected to a mass embedded in a finite truss of elastic rods. There, we also provide illustrative examples that demonstrate how the model can be used to characterise the transient behaviour of the system. Moreover, to check the validity of the formulation, we compare the analytical results with the numerical outcomes obtained from an independent finite element model. In Section 3, we consider periodic elastic systems connected to arrays of gyroscopic spinners. Specifically, we focus on a triangular elastic medium connected to two types of spinners and show how to realise highly localised waveforms in this medium in the transient regime. The second problem considered involves a gyro-elastic hexagonal lattice containing an interface defined by a heterogeneous system of spinners and we provide transient simulations demonstrating how to produce unidirectional interfacial waves. In Section 4, two important applications for a hexagonal gyro-elastic lattice are presented. First, we discuss the problem of topological protection in a lattice with a hexagonal domain that contains a cavity and is excited on the exterior boundary. There, unidirectional edge waves travel along the external boundary of the lattice, leaving the interior almost undisturbed. Second, we design a discrete gyro-elastic invisibility cloak, which is capable of hiding a defect in a periodic structured medium. In Section 5 we provide some concluding remarks. In the appendices, we give additional details on the angular momentum balance of the gyroscopic spinner and on the dispersion relations of the elastic lattices considered in this paper.

2. Motion of the gyroscopic oscillator

In this section, we study the transient motion of a single gyroscopic spinner that is hinged at its base and connected to a mass at its tip. The mass m is elastically constrained by a system of six extensional springs having stiffness c (see Fig. 3(a)). The effect of gravity will be neglected throughout.

2.1. Non-linear governing equations of the gyroscopic spinner

The generalised coordinates or Euler angles (Goldstein, Poole, & Safko, 2001) that describe the motion of the gyroscopic spinner are denoted by ϕ, θ and ψ, and represent the precession, nutation and spin angle of the gyroscopic spinner, respectively. They are shown in Fig. 3(b).

(a) (b) (c)
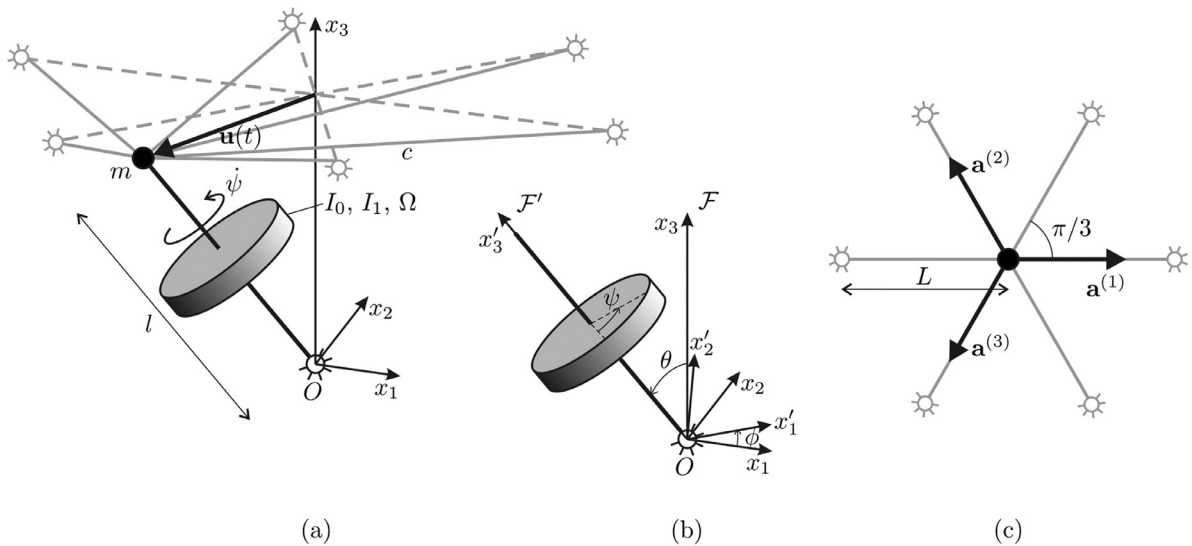
Fig. 3. The gyroscopic oscillator. (a) A gyroscopic spinner hinged at its base and having a spin rate $\dot{\psi}$. At the top of the spinner a concentrated mass m is constrained by six non-inertial truss elements depicted in grey and having stiffness c. The mass displacement is $\mathbf{u}(t)$. The spinner has length l, moments of inertia I_0 and I_1, and gyricity Ω. (b) The Euler angles: precession ϕ, nutation θ and spin ψ of the gyroscopic spinner. In addition, the fixed frame $\mathcal{F}$ with coordinate system $Ox_1x_2x_3$ and the moving frame $\mathcal{F}'$ with coordinate system $Ox_1'x_2'x_3'$ are shown. The frame $\mathcal{F}'$ precesses with angle ϕ and nutates with angle θ. (c) Planar view in the reference configuration. The extensional springs have initial length L, and the basis vectors for the in-plane elastic system are $\mathbf{a}^{(1)}$, $\mathbf{a}^{(2)}$ and $\mathbf{a}^{(3)}$.

The angular momentum balance for the spinner takes the form

$$\mathbf{M}_{\mathrm{e}} = \frac{\mathrm{d}}{\mathrm{d}t}(\mathbf{I}_{\mathrm{g}}\boldsymbol{\omega}_{\mathrm{g}}), \tag{1}$$

where $\mathbf{M}_{\mathrm{e}}$ represents the vector of external moments applied to the spinner, and $\mathbf{I}_{\mathrm{g}}$ and $\boldsymbol{\omega}_{\mathrm{g}}$ denote the spinner's moment of inertia tensor and angular velocity vector, respectively (see Brun et al., 2012; Carta et al., 2018; Goldstein et al., 2001; Nieves et al., 2018). Due to the axial symmetry of the spinner with respect to the moving frame $\mathcal{F}'$, the tensor $\mathbf{I}_{\mathrm{g}}$ is diagonal and is assumed to have the form

$$\mathbf{I}_{\mathrm{g}} = I_0(\mathbf{e}_1' \otimes \mathbf{e}_1' + \mathbf{e}_2' \otimes \mathbf{e}_2') + I_1 \mathbf{e}_3' \otimes \mathbf{e}_3'. \tag{2}$$

The angular velocity of the gyroscopic spinner $\boldsymbol{\omega}_{\mathrm{g}}$ is conveniently expressed in terms of Euler angles. The full derivation is reported in Appendix A, where it is shown that the angular momentum balance (1) in fixed coordinates $(Ox_1x_2x_3)$ is given by the following system of non-linear ordinary differential equations

$$M_1 = I_0 \frac{\mathrm{d}}{\mathrm{d}t}[-\dot{\phi}\sin(\phi)\sin(\theta)\cos(\theta) + \dot{\theta}\cos(\phi)] + I_1 \frac{\mathrm{d}}{\mathrm{d}t}[\sin(\theta)\sin(\phi)(\dot{\phi}\cos(\theta) + \dot{\psi})],$$
$$M_2 = I_0 \frac{\mathrm{d}}{\mathrm{d}t}[\dot{\phi}\cos(\phi)\sin(\theta)\cos(\theta) + \dot{\theta}\sin(\phi)] - I_1 \frac{\mathrm{d}}{\mathrm{d}t}[\sin(\theta)\cos(\phi)(\dot{\phi}\cos(\theta) + \dot{\psi})],$$
$$M_3 = I_0 \frac{\mathrm{d}}{\mathrm{d}t}(\dot{\phi}\sin^2(\theta)) + I_1 \frac{\mathrm{d}}{\mathrm{d}t}[\cos(\theta)(\dot{\psi} + \dot{\phi}\cos(\theta))]. \tag{3}$$

2.1.1. External actions on the gyroscopic spinner

The position vector of the mass m is

$$\boldsymbol{l}(t) = l\sin(\theta(t))\sin(\phi(t))\mathbf{e}_1 - l\sin(\theta(t))\cos(\phi(t))\mathbf{e}_2 + l\cos(\theta(t))\mathbf{e}_3, \tag{4}$$

where l is the length of the spinner (see Fig. 3(a)). The mass displacement is $\mathbf{u}(t) = \boldsymbol{l}(t) - \boldsymbol{l}(0)$, and we assume that $\boldsymbol{l}(0) = l\mathbf{e}_3$.

At the tip of the gyroscopic spinner, there acts the force

$$\mathbf{F} = -c\,\mathbf{h}[\mathbf{u}(t)] - m\ddot{\mathbf{u}}(t), \tag{5}$$

which embeds the inertia term brought by the mass m and the elastic reaction of the extensional springs of stiffness c, described by the non-linear vectorial function $\mathbf{h}$. Using the basis vectors

$$\mathbf{a}^{(i)} = \cos\left((i-1)\frac{2\pi}{3}\right)\mathbf{e}_1 + \sin\left((i-1)\frac{2\pi}{3}\right)\mathbf{e}_2, \qquad i = 1, 2, 3, \tag{6}$$

shown in Fig. 3(c), the function $\mathbf{h}$ can be computed as

$$\mathbf{h} = \sum_{i=1}^{3}\left[(|\mathbf{u}(t) - L\mathbf{a}^{(i)}| - L)\frac{\mathbf{u}(t) - L\mathbf{a}^{(i)}}{|\mathbf{u}(t) - L\mathbf{a}^{(i)}|} + (|\mathbf{u}(t) + L\mathbf{a}^{(i)}| - L)\frac{\mathbf{u}(t) + L\mathbf{a}^{(i)}}{|\mathbf{u}(t) + L\mathbf{a}^{(i)}|}\right], \tag{7}$$

where L is the initial length of the extensional springs (see Fig. 3(c)).

The corresponding external moment acting on the gyroscopic spinner is

$$\mathbf{M}_{\mathrm{e}} = \boldsymbol{l} \times \mathbf{F}. \tag{8}$$

2.1.2. Normalisation

Next, we introduce the normalisations

$$\tilde{\boldsymbol{l}} = \frac{\boldsymbol{l}}{l}, \quad \tilde{t} = \sqrt{\frac{c}{m\gamma}}t, \quad \gamma = 1 + \frac{I_0}{ml^2}, \quad \delta = \frac{l}{L}, \quad \tilde{\mathbf{u}}(\tilde{t}) = \frac{\mathbf{u}(t)}{L},$$

$$\tilde{\mathbf{h}}[\tilde{\mathbf{u}}] = \frac{\mathbf{h}[\mathbf{u}]}{L}, \quad \tilde{\mathbf{F}} = \frac{\mathbf{F}}{cL}, \quad \tilde{\mathbf{M}}_{\mathrm{e}} = \frac{\mathbf{M}_{\mathrm{e}}}{cLl}, \quad \tilde{I}_j = \frac{I_j}{mlL} \quad (j = 0, 1), \tag{9}$$

where the quantities with the symbol "˜" are dimensionless.

In the following we omit the symbol "˜" for ease of notation. We will also use the same notations for the Euler angles but assume these are now functions of the dimensionless time. After employing the previous normalisations, we obtain from (3) and (8)

$$M_1 = -\cos(\theta)F_2 - \cos(\phi)\sin(\theta)F_3$$
$$= \frac{I_0}{\gamma}\frac{d}{dt}[-\dot{\phi}\sin(\phi)\sin(\theta)\cos(\theta) + \dot{\theta}\cos(\phi)] + \frac{I_1}{\gamma}\frac{d}{dt}[\sin(\theta)\sin(\phi)(\dot{\phi}\cos(\theta) + \dot{\psi})],$$
$$M_2 = \cos(\theta)F_1 - \sin(\phi)\sin(\theta)F_3$$
$$= \frac{I_0}{\gamma}\frac{d}{dt}[\dot{\phi}\cos(\phi)\sin(\theta)\cos(\theta) + \dot{\theta}\sin(\phi)] - \frac{I_1}{\gamma}\frac{d}{dt}[\sin(\theta)\cos(\phi)(\dot{\phi}\cos(\theta) + \dot{\psi})] \tag{10}$$

and

$$M_3 = \sin(\theta)[\cos(\phi)F_1 + \sin(\phi)F_2]$$
$$= \frac{I_0}{\gamma}\frac{d}{dt}[\dot{\phi}\sin^2(\theta)] + \frac{I_1}{\gamma}\frac{d}{dt}[\cos(\theta)(\dot{\psi} + \dot{\phi}\cos(\theta))]. \tag{11}$$

Furthermore, (5) is updated to

$$\mathbf{F} = -\mathbf{h}[\mathbf{u}(t)] - \gamma^{-1}\ddot{\mathbf{u}}(t). \tag{12}$$

2.2. The linearised problem

We now assume that the nutation angle and its time derivatives satisfy

$$\left|\frac{d^j\theta(t)}{dt^j}\right| \le \text{Const } \varepsilon, \qquad j = 0, 1, 2,$$

where ε is a small dimensionless quantity such that $0 < \varepsilon \ll 1$.

Linearising (11) with respect to the nutation angle yields

$$\gamma\theta(F_2\sin(\phi) + F_1\cos(\phi)) + O(\varepsilon^3\gamma(|F_1| + |F_2|))$$
$$= I_1(\ddot{\psi} + \ddot{\phi}) + O(I_1\varepsilon^2(|\dot{\psi} + \dot{\phi}| + |\ddot{\psi} + \ddot{\phi}|)) + O((I_1 + I_0)\varepsilon^2(|\dot{\phi}| + |\ddot{\phi}|)). \tag{13}$$

It also follows from (4) that $u_3 = O(\varepsilon^2)$. In addition, the function $\mathbf{h}[\mathbf{u}(t)]$ in (7) can be linearised so that (12) becomes

$$\mathbf{F} = -\mathbf{K}\mathbf{u}(t) - \gamma^{-1}\ddot{\mathbf{u}}(t) + O(\varepsilon^2\delta(\delta + \gamma^{-1})), \tag{14}$$

where $\mathbf{K}$ is the stiffness matrix characterising the action of the springs. We note in (14) that $F_3 = O(\varepsilon^2\delta(\delta + \gamma^{-1}))$. As a result, in going forward we neglect the $\mathbf{e}_3$ component of the motion for the mass and set $\mathbf{F} = (F_1, F_2)^T$ and $\mathbf{u} = (u_1, u_2)^T$. Moreover, the stiffness matrix $\mathbf{K}$ in (14) takes the form

$$\mathbf{K} = 2\sum_{j=1}^{3}\mathbf{a}^{(j)}\otimes\mathbf{a}^{(j)} = 3\mathbf{I}_2, \tag{15}$$

where $\mathbf{I}_2$ is the 2×2 identity matrix.

We now derive the form of the in-plane forces acting on the mass. Due to the smallness of F_3 its contribution to M_1 and M_2 in Eq. (10) can be neglected. Accordingly, after introducing the normalised forms of the displacements u_1 and u_2, we rewrite Eq. (10) as

$$F_1 = \frac{1}{\gamma\cos(\theta)}\left[I_0\frac{d}{dt}\left(\frac{\dot{u}_1}{\delta}\cos(\theta) + \dot{\theta}\sin^2(\theta)\sin(\phi)\right) + \frac{I_1}{\delta}\frac{d}{dt}((\dot{\phi}\cos(\theta) + \dot{\psi})u_2)\right] + O\left(\varepsilon^3\delta\left(\delta + \frac{1}{\gamma}\right)\right),$$
$$F_2 = \frac{1}{\gamma\cos(\theta)}\left[I_0\frac{d}{dt}\left(\frac{\dot{u}_2}{\delta}\cos(\theta) - \dot{\theta}\sin^2(\theta)\cos(\phi)\right) - \frac{I_1}{\delta}\frac{d}{dt}((\dot{\phi}\cos(\theta) + \dot{\psi})u_1)\right] + O\left(\varepsilon^3\delta\left(\delta + \frac{1}{\gamma}\right)\right). \tag{16}$$

Carrying out the linearisation with respect to the nutation angle once more shows that

$$F_1 = \frac{I_0}{\gamma\delta}\ddot{u}_1 + \frac{I_1}{\gamma\delta}[(\ddot{\psi} + \ddot{\phi})u_2 + (\dot{\psi} + \dot{\phi})\dot{u}_2] + O\left(\frac{(I_0 + I_1)}{\gamma}\varepsilon^3(|\dot{\phi}| + |\dot{\phi}|^2 + |\ddot{\phi}|)\right) + O\left(\frac{I_0}{\gamma}\varepsilon^3\right) + O\left(\frac{I_1}{\gamma}\varepsilon^3|\ddot{\phi} + \ddot{\psi}|\right)$$
$$O\left(\frac{I_1}{\gamma}\varepsilon^3(1 + |\dot{\phi}|)(|\dot{\phi} + \dot{\psi}|)\right) + O\left(\varepsilon^3\delta\left(\delta + \frac{1}{\gamma}\right)\right),$$
$$F_2 = \frac{I_0}{\gamma\delta}\ddot{u}_2 - \frac{I_1}{\gamma\delta}[(\ddot{\psi} + \ddot{\phi})u_1 + (\dot{\psi} + \dot{\phi})\dot{u}_1] + O\left(\frac{(I_0 + I_1)}{\gamma}\varepsilon^3(|\dot{\phi}| + |\dot{\phi}|^2 + |\ddot{\phi}|)\right) + O\left(\frac{I_0}{\gamma}\varepsilon^3\right) + O\left(\frac{I_1}{\gamma}\varepsilon^3|\ddot{\phi} + \ddot{\psi}|\right)$$
$$O\left(\frac{I_1}{\gamma}\varepsilon^3(1 + |\dot{\phi}|)(|\dot{\phi} + \dot{\psi}|)\right) + O\left(\varepsilon^3\delta\left(\delta + \frac{1}{\gamma}\right)\right). \tag{17}$$

The last two equalities lead to

$$\gamma F_j = O(\varepsilon I_0[(1 + |\dot{\phi}|)^2 + |\ddot{\phi}|]) + O(\varepsilon I_1(|\dot{\psi} + \dot{\phi}|(1 + |\dot{\phi}|) + |\ddot{\psi} + \ddot{\phi}|)), \tag{18}$$

for $j = 1, 2$. Returning to (13), we have

$$0 = I_1(\ddot{\psi} + \ddot{\phi}) + O(I_0\varepsilon^2(1 + |\dot{\phi}|^2)) + O((I_1 + I_0)\varepsilon^2(|\dot{\phi}| + |\ddot{\phi}|)) + O(I_1\varepsilon^2(|\dot{\psi} + \dot{\phi}|(1 + |\dot{\phi}|) + |\ddot{\psi} + \ddot{\phi}|)), \tag{19}$$

which implies that, to leading order, the sum of the precession and spin rates is independent of time. Therefore, we define

$$\Omega = \dot{\psi}(0) + \dot{\phi}(0) = \dot{\psi}(t) + \dot{\phi}(t). \tag{20}$$

From here on, Ω is referred to as the *gyricity* of the gyroscopic spinner. In this case, (19) is satisfied if the gyricity Ω, the precession and its time derivatives do not compete with ε. Here the gyricity is given in normalised form; the normalisation factor is $\sqrt{m\gamma/c}$, and the dimension is radians per unit time. We note that although the gyricity is constant throughout the motion of the spinner, the spin and precession rates can change with time and in general are not constant. This fact is further illustrated in Section 2.3.

2.2.1. Linearised governing equations for the mass

The linearised equations for the mass m are obtained by combining (17) with (14) and (15). In doing so, to leading order one can obtain the governing equation for the mass as

$$\ddot{\mathbf{u}}(t) + \alpha\Omega\mathbf{R}\dot{\mathbf{u}}(t) + 3\mathbf{u}(t) = \mathbf{0}, \tag{21}$$

where now $\mathbf{u} = (u_1, u_2)^\mathsf{T}$. In addition,

$$\alpha = \frac{I_1}{(\delta + I_0)} \quad \text{and} \quad \mathbf{R} = \begin{pmatrix} 0 & 1 \\ -1 & 0 \end{pmatrix}. \tag{22}$$

In (21) the matrix $\mathbf{R}$ provides the coupling of the in-plane components of the displacement of the mass, and the intensity of this is determined by the parameters α and Ω characterising the gyroscope and its motion. The result (21) also illustrates that the gyricity Ω is a fundamental quantity in characterising how a gyroscopic spinner interacts with an elastic system and we refer to Carta et al. (2018), Nieves et al. (2018), where this quantity also appears in the modelling of other systems composed of spinners connected to Euler-Bernoulli beams.

2.3. Transient motion of the gyroscopic oscillator

In the small nutation regime, the motion is governed by Eq. (21), where the skew-symmetric matrix $\mathbf{R}$ describes the chiral effect induced by the gyroscopic spinner.

One can construct the solution of (21) through a modal analysis by studying the existence of solutions in the form

$$\mathbf{u}(t) = \mathbf{A}e^{i\omega t}, \tag{23}$$

where the constant amplitude vector $\mathbf{A}$ and the radian frequency ω should be determined. Insertion of (23) into (21) leads to the homogeneous system

$$\begin{pmatrix} -\omega^2 + 3 & i\alpha\Omega\omega \\ -i\alpha\Omega\omega & -\omega^2 + 3 \end{pmatrix} \mathbf{A} = \mathbf{0}. \tag{24}$$

Non-trivial solutions $\mathbf{A}$ of this system are obtained by analysing when the determinant of the preceding Hermitian matrix vanishes:

$$(3 - \omega^2)^2 - (\alpha\Omega\omega)^2 = 0. \tag{25}$$

The positive solutions of the equation above are

$$\omega_\pm = \frac{1}{2}\left[\pm\alpha\Omega + \sqrt{(\alpha\Omega)^2 + 12}\right]. \tag{26}$$

We also write the non-trivial vector $\mathbf{A}$ in the form

$$\mathbf{A}(\omega) = \begin{pmatrix} 1 \\ i\frac{3 - \omega^2}{\alpha\Omega\omega} \end{pmatrix}. \tag{27}$$

Next, we consider some numerical illustrations of the solution obtained for a system with the parameter $\alpha = 0.25$. The frequencies (26) are plotted as functions of the gyricity Ω in Fig. 4, where it can be seen that one frequency is monotonically increasing while the other is monotonically decreasing. When the gyricity is zero, we have a double eigenfrequency for the system; in this case, the gyroscope does neither spin nor precess during its motion. In addition, in Fig. 4 we show the vertical dashed line for the gyricity $\Omega = 6$, where the two eigenfrequencies are $\omega_+ = 2.6375$ and $\omega_- = 1.1375$. These values will be used in the numerical results presented below.
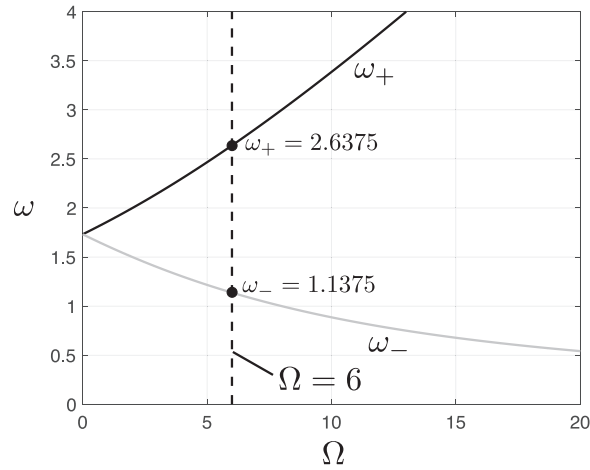
Fig. 4. Eigenfrequencies of the gyroscopic oscillator in Fig. 3 as a function of the gyricity Ω. Computations are based on (26), with the parameter $\alpha = 0.25$. The dashed line indicates the case $\Omega = 6$, considered in Figs. 5 and 6. The values of $\omega_\pm$ in (26) when $\Omega = 6$ are also shown.

(a)   (b)
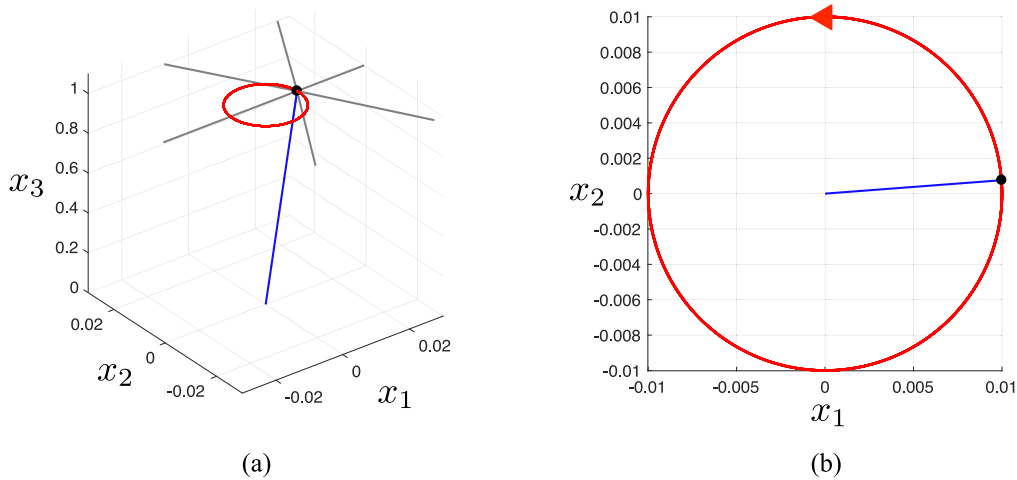
Fig. 5. Motion of the gyroscopic oscillator shown in Fig. 3. The result corresponds to gyricity $\Omega = 6$, $\alpha = 0.25$ and initial conditions (29)–(31). (a) The linearised motion of the mass m in the time interval $0 \leq t \leq 2.42$ is given in red. Note the different scales used for the plane (x_1, x_2) and the axis x_3. (b) Planar view of the trajectory traced by the mass m, where the direction of the motion of the mass is indicated with the arrow. The behaviour of the system is further illustrated in Video 3 of the Supplementary Material. (For interpretation of the references to colour in this figure, the reader is referred to the web version of this article.)

In general, the motion of the system can be written as a linear combination of modes of the form (23), with (27), so that the solution $\mathbf{u}$ of (21) is

$$\mathbf{u}(t) = c_1 \mathbf{A}(\omega_+) e^{i\omega_+ t} + c_2 \overline{\mathbf{A}(\omega_+)} e^{-i\omega_+ t} + c_3 \mathbf{A}(\omega_-) e^{i\omega_- t} + c_4 \overline{\mathbf{A}(\omega_-)} e^{-i\omega_- t}, \tag{28}$$

where the constant coefficients c_1, c_2, c_3 and c_4 are determined from the initial conditions for the system.

The mode corresponding to the eigenfrequency $\omega_+ = 2.6375$, obtained for $\Omega = 6$, assuming $\delta = 1$, is shown in Fig. 5, where the mass moves anticlockwise along a circular trajectory with radius 0.01 and centre at the origin. This is further illustrated in Video 3 in the Supplementary Material, where it can be seen that the normalised period is $2\pi/\omega_+ = 2.3823$. The motion of the system coincides with the mode corresponding to the frequency ω_+ if one sets the initial conditions of the system as

$$\mathbf{u}(0) = \begin{pmatrix} 0.01 \\ 0 \end{pmatrix}, \quad \dot{\mathbf{u}}(0) = \begin{pmatrix} 0 \\ 0.0264 \end{pmatrix}. \tag{29}$$

This initial data is associated with the following initial conditions for the precession, nutation and spin of the spinner:

$$\phi(0) = \pi/2, \quad \dot{\phi}(0) = 2.6375, \quad \theta(0) = 0.01, \quad \dot{\theta}(0) = 0, \tag{30}$$
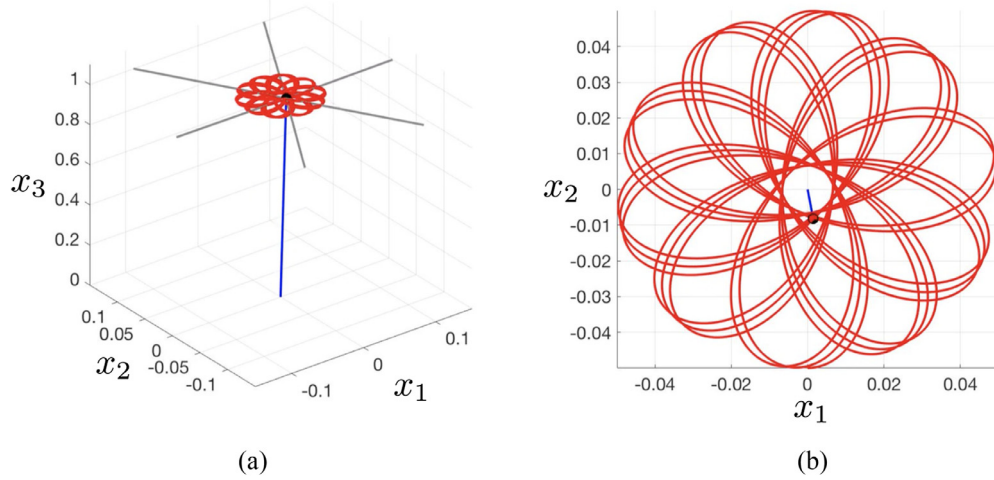
Fig. 6. Motion of the gyroscopic oscillator shown in Fig. 3. The result corresponds to the same parameters of Fig. 5, but initial conditions (32)–(34). (a) The trajectory of the mass m in the time interval $0 \leq t \leq 47.5$ is given in red. (b) Planar view of the trajectory traced by the mass m. The motion of the system is further illustrated in Video 4 of the Supplementary Material. (For interpretation of the references to colour in this figure, the reader is referred to the web version of this article.)

and

$$\psi(0) = 0, \quad \dot{\psi}(0) = \Omega - \dot{\phi}(0) = 3.3625. \tag{31}$$

For the mode corresponding to $\omega_- = 1.1375$, the mass m moves clockwise on a circular trajectory, with a normalised period $2\pi/\omega_- = 5.5239$. We note that in association with the eigenmodes the precession and spin rates of the spinner are constant and these quantities sum to give the prescribed value of the gyricity, in this case $\Omega = 6$.

As an illustration showing a more general motion of the system that combines the modes corresponding to both frequencies $\omega_\pm$, we set the initial conditions as

$$\mathbf{u}(0) = \begin{pmatrix} 0 \\ -0.05 \end{pmatrix}, \quad \dot{\mathbf{u}}(0) = \begin{pmatrix} 0.05 \\ 0 \end{pmatrix}. \tag{32}$$

These can be linked to the following initial data for the generalised coordinates of the spinner:

$$\phi(0) = 0, \quad \dot{\phi}(0) = 1, \quad \theta(0) = 0.05, \quad \dot{\theta}(0) = 0, \tag{33}$$

and

$$\psi(0) = 0, \quad \dot{\psi}(0) = \Omega - \dot{\phi}(0) = 5. \tag{34}$$

As shown in Fig. 6, the trajectory traced by the mass is non-circular and is contained inside an annulus with the origin as its centre and its inner and outer radii approximately equal to 0.007 and 0.05, respectively. This motion results from the combination of both modes of the system and can be further examined in Video 4 of the Supplementary Material. There, it is clear that the precession rate of the spinner is not constant and hence its spin rate is also dependent on time. However, as shown in Section 2.2 the sum of these quantities is constant.

As mentioned above, the behaviour of the system can allow for a variety of trajectories for the mass. As an additional example of this, we refer to Fig. 1, which was computed for the parameters and initial conditions specified in the caption of Fig. 6, except that $\alpha = 1$. The motion is also reported in Video 1 of the Supplementary Material.

2.4. Finite element simulation

Here, we compare the analytical results based on (21) with the numerical outcomes obtained from a finite element simulation developed in *Comsol Multiphysics 5.3*.

A non-linear transient analysis has been performed based on the model shown in Fig. 7. The gyroscopic spinner is implemented as a solid rigid body, the mass m as a cylindrical rigid element of small size and six truss elements represent the extensional springs. The values of the material and geometrical parameters are given in the caption of Fig. 7. The normalised values are the following: $I_0 = 0.637$, $I_1 = 0.1$, $\gamma = 1.637$ and $\alpha = 0.061$.

The following normalised initial conditions have been imposed:

$$\phi(0) = \theta(0) = \psi(0) = 0, \quad \dot{\theta}(0) = 0.040, \quad \dot{\phi}(0) = \dot{\psi}(0) = 101.15, \tag{35}$$
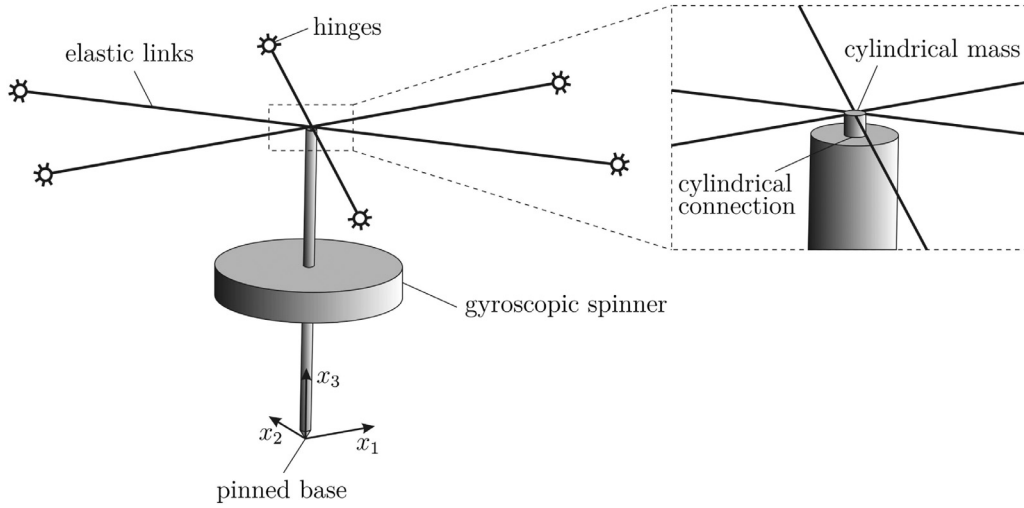
Fig. 7. The geometry of the model implemented in *Comsol*, consisting of a gyroscopic spinner (represented by a rigid solid) that is pinned at the base and whose tip is connected to a mass m (represented by a small cylinder), that is also connected to an array of six extensional springs (shown as lines). The gyroscopic spinner has moments of inertia 63.7 kg m^2 about the $x_{1,2}$-axes and 10.0 kg m^2 about the x_3-axis, respectively, and the length $l = 1$ m. The initial spin and precession rates are $\dot{\psi} = \dot{\phi} = 250$ rad/s. The mass at the tip of the spinner is $m = 100$ kg. Each rod has longitudinal stiffness $c = 1000$ N m^{-1} and length $L = 1$ m.
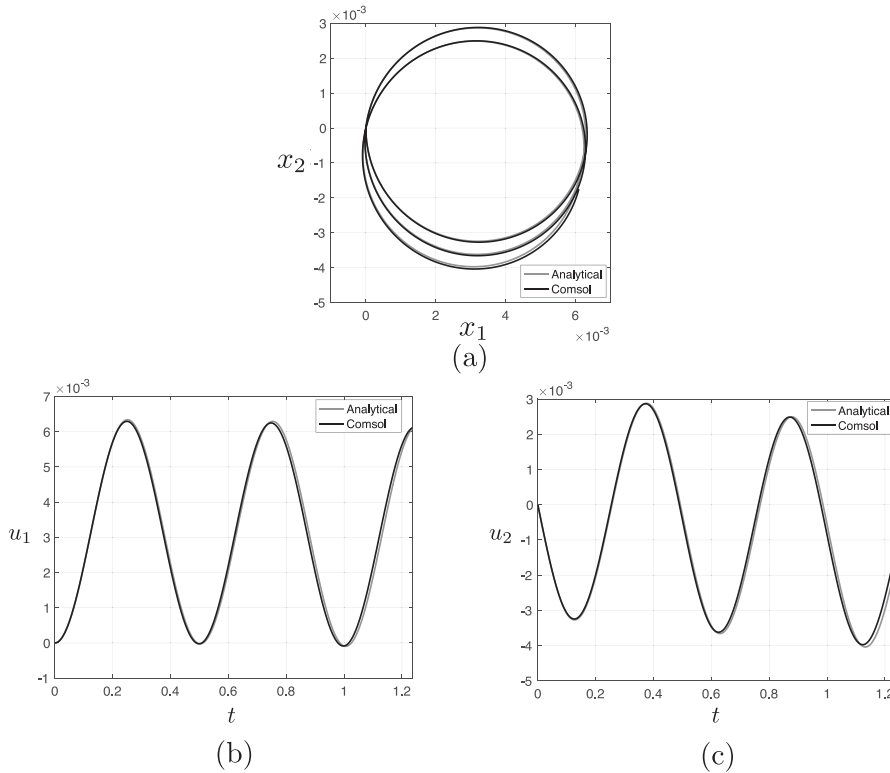
Fig. 8. (a) The trajectory traced by the mass in the system shown in Fig. 7, resulting from a transient analysis in *Comsol*, and the comparison with the analytical results. Displacements (b) u_1 and (c) u_2 of the mass m as a function of time.

which correspond to the gyricity $\Omega = 202.30$ and

$$\mathbf{u}(0) = \begin{pmatrix} 0 \\ 0 \end{pmatrix}, \quad \dot{\mathbf{u}}(0) = \begin{pmatrix} 0 \\ -0.040 \end{pmatrix}. \tag{36}$$

The results of the transient simulation are shown in Fig. 8 together with the analytical ones. It is evident that the numerical results obtained from a non-linear transient simulation in *Comsol* are in excellent agreement with the analytical predictions. The results confirm the correctness of the analytical approach and the validity of the proposed linearisation.

Once again, the motion shown in Fig. 8 demonstrates the coupling effect induced by the spin and precession rates of the spinner. Despite the fact that the initial conditions (36) excite the motion only in direction x_2, both displacement components u_1 and u_2 vary sinusoidally with similar amplitude.

The model developed here extends the results previously reported in Brun et al. (2012), in addition to providing the first comparison between analytical and independent numerical models.

3. Transient analysis of gyro-elastic lattices

In this section, we extend the theoretical results of Section 2 to model the interaction of masses, placed at the junctions of various lattice systems that are connected to inhomogeneous arrays of spinners. The inhomogeneity will be associated with a non-constant distribution of the parameter α or the gyricity constant Ω. In addition, for some of the examples considered below, the gyricity constant in the gyro-elastic lattice will be chosen as $|\Omega| = \omega$, where ω is the radian frequency of vibration of the lattice particles (see Brun et al., 2012; Carta et al., 2014; Carta et al., 2017a; Garau et al., 2018 where such cases are analysed). On the other hand, for some of the problems considered, we provide examples where the gyricity will be taken as a parameter independent of the radian frequency of the lattice. In those cases, we will also find that the desired dynamic effects can be retrieved.

The steady-state analyses presented in Carta et al. (2017a) and Garau et al. (2018) have shown that the gyro-elastic lattice may lead to special waveforms due to the dynamic chirality conferred by the spinners to the lattice. In this paper, we investigate several possibilities that also allow these special waveforms to appear in the transient regime. In addition, the transient analysis may bring new interesting dynamic features that cannot be revealed through a steady-state analysis. Moreover, in some cases we will study the response of the gyro-elastic systems for different initial conditions or when subjected to fully transient loads.

3.1. Localised waveforms

We consider a periodic triangular lattice as shown in Fig. 9, composed of masses m periodically constrained by elastic links having stiffness c and length L. Each mass is attached to a gyroscopic spinner that spins about its axis parallel to $0x_3$. The spinners have normalised parameters α_A or α_B, and alternating gyricities $\Omega = \pm\omega$ as shown in Fig. 9. The unit cell of the periodic system contains two nodal points, and the lattice basis vectors are $\mathbf{t}^{(1)} = (2, 0)^{\mathrm{T}}$ and $\mathbf{t}^{(2)} = (1/2, \sqrt{3}/2)^{\mathrm{T}}$. Each unit cell is identified by the multi-index $\mathbf{n} = (n_1, n_2)^{\mathrm{T}}$ and the displacements of the two nodes within each cell are indicated with $\mathbf{u}_A^{(\mathbf{n})} = \mathbf{u}_A^{(n_1, n_2)}$ and $\mathbf{u}_B^{(\mathbf{n})} = \mathbf{u}_B^{(n_1, n_2)}$.

Following the theoretical model developed in Section 2 and assuming nearest neighbour interactions only, the linearised governing equations of the lattice are

$$\ddot{\mathbf{u}}_A^{(n_1,n_2)} = \left[\mathbf{a}^{(1)} \cdot \left(\mathbf{u}_B^{(n_1,n_2)} + \mathbf{u}_B^{(n_1-1,n_2)} - 2\mathbf{u}_A^{(n_1,n_2)} \right) \mathbf{a}^{(1)} + \mathbf{a}^{(2)} \cdot \left(\mathbf{u}_B^{(n_1-1,n_2+1)} + \mathbf{u}_B^{(n_1,n_2-1)} - 2\mathbf{u}_A^{(n_1,n_2)} \right) \mathbf{a}^{(2)} \right.$$
$$\left. + \mathbf{a}^{(3)} \cdot \left(\mathbf{u}_A^{(n_1,n_2+1)} + \mathbf{u}_A^{(n_1,n_2-1)} - 2\mathbf{u}_A^{(n_1,n_2)} \right) \mathbf{a}^{(3)} \right] - \alpha_A \omega \mathbf{R} \dot{\mathbf{u}}_A^{(n_1,n_2)}, \tag{37}$$

$$\ddot{\mathbf{u}}_B^{(n_1,n_2)} = \left[\mathbf{a}^{(1)} \cdot \left(\mathbf{u}_A^{(n_1+1,n_2)} + \mathbf{u}_A^{(n_1,n_2)} - 2\mathbf{u}_B^{(n_1,n_2)} \right) \mathbf{a}^{(1)} + \mathbf{a}^{(2)} \cdot \left(\mathbf{u}_A^{(n_1,n_2+1)} + \mathbf{u}_A^{(n_1+1,n_2-1)} - 2\mathbf{u}_B^{(n_1,n_2)} \right) \mathbf{a}^{(2)} \right.$$
$$\left. + \mathbf{a}^{(3)} \cdot \left(\mathbf{u}_B^{(n_1,n_2+1)} + \mathbf{u}_B^{(n_1,n_2-1)} - 2\mathbf{u}_B^{(n_1,n_2)} \right) \mathbf{a}^{(3)} \right] + \alpha_B \omega \mathbf{R} \dot{\mathbf{u}}_B^{(n_1,n_2)}, \tag{38}$$

where the basis vectors $\mathbf{a}^{(j)}$, $j = 1, 2, 3$, shown in Fig. 3(c), were given in (6). The last terms appearing in the right-hand sides of Eqs. (37) and (38) represent the influence of two different spinners in the unit cell having gyricities of equal magnitude but opposite sign, i.e., $\Omega_A = -\Omega_B = \omega$.
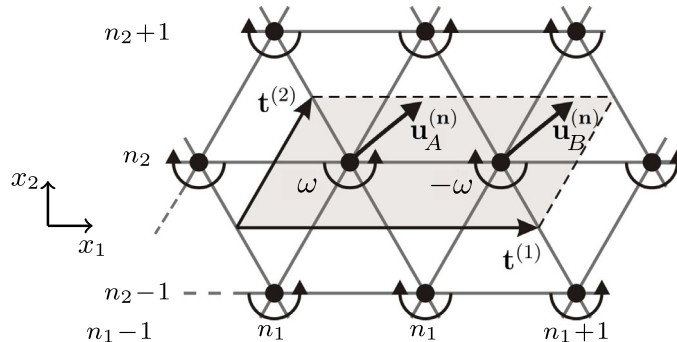
Fig. 9. Infinite triangular elastic lattice attached to an array of gyroscopic spinners. Masses m at the nodal points are connected by extensional springs of stiffness c and length L. The unit cell of the periodic system is indicated in grey and it is defined by the vectors $\mathbf{t}^{(1)} = (2, 0)^{\mathrm{T}}$ and $\mathbf{t}^{(2)} = (1/2, \sqrt{3}/2)^{\mathrm{T}}$. Nodal points are identified by the multi-index $\mathbf{n} = (n_1, n_2)^{\mathrm{T}}$. The gyricity Ω has magnitude ω and alternates in sign switching from A to B.

### 3.1.1. Generation of localised waveforms in the transient regime

In Carta et al. (2017a) it was demonstrated that waveforms localised in a single line can be created at specific frequencies in a gyro-elastic lattice with two types of spinners, shown in Fig. 9. This phenomenon is associated with the dispersion properties of the structured medium.

The derivation of the dispersion properties for such a system is reported in Appendix B. In Fig. 10(a) we show the dispersion surfaces obtained from (B.3), where $\alpha_A = 0.8$ and $\alpha_B = 0.9$. The slowness contours at $\omega = 1.717\,\pi = 5.394$ are given in Fig. 10(b). The first Brillouin zone is also indicated, defined by the reciprocal vectors

$$\mathbf{b}^{(1)} = (\pi, -\pi/\sqrt{3}), \qquad \mathbf{b}^{(2)} = (0, 4\pi/\sqrt{3}). \tag{39}$$

The slowness contours are associated with wave propagation in the direction normal to the contour lines, namely $(1/2, \sqrt{3}/2)$.

In Fig. 11 we show the results of a transient analysis, which is performed on a finite lattice with dimensions $100 \times 50\sqrt{3}$. A *Matlab* code has been implemented in order to solve the equations of motion (37) and (38) on the 5000 unit cells of
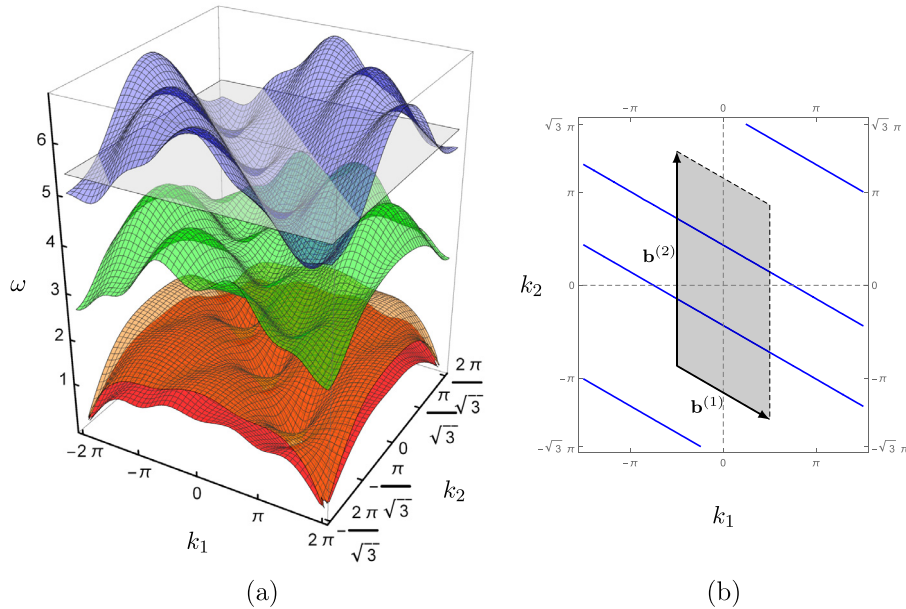
Fig. 10. Dispersion properties of the gyro-elastic lattice in Fig. 9. The computations are given for $\alpha_A = 0.8$ and $\alpha_B = 0.9$. (a) Dispersion surfaces. (b) Slowness contours at $\omega = 1.72\,\pi = 5.39$. These contours are associated with the propagation of localised waves in the direction $(1/2, \sqrt{3}/2)$. The grey region represents the first Brillouin zone. (For interpretation of the references to colour in this figure, the reader is referred to the web version of this article.)
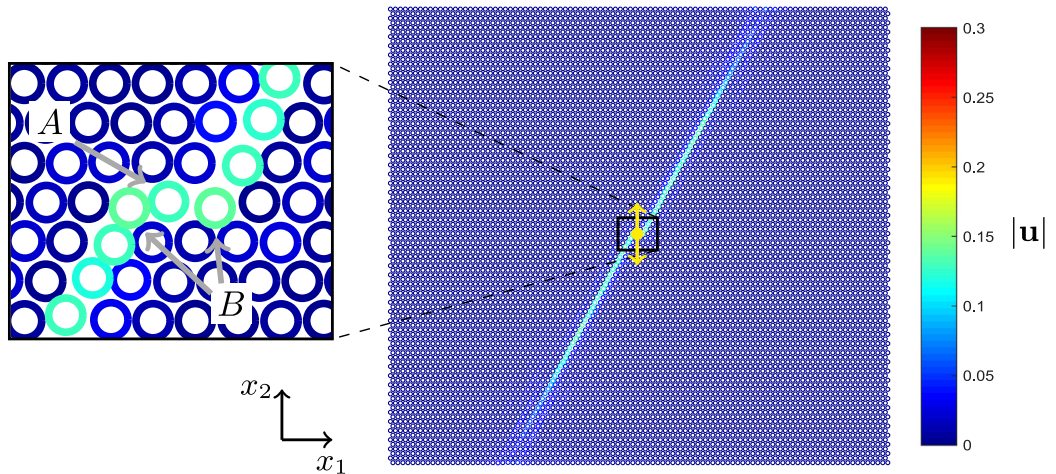
Fig. 11. Transient dynamic analysis in a finite gyro-elastic lattice composed of 5000 unit cells with spinners possessing $\alpha_A = 0.8$, $\alpha_B = 0.9$ and gyricities $\Omega_A = -\Omega_B = \omega = 1.72\pi$. The displacement magnitude $|\mathbf{u}|$ is given at the normalised time $t = 233.58$. The full transient solution is illustrated in Video 5 of the Supplementary Material. (For interpretation of the references to colour in this figure, the reader is referred to the web version of this article.)
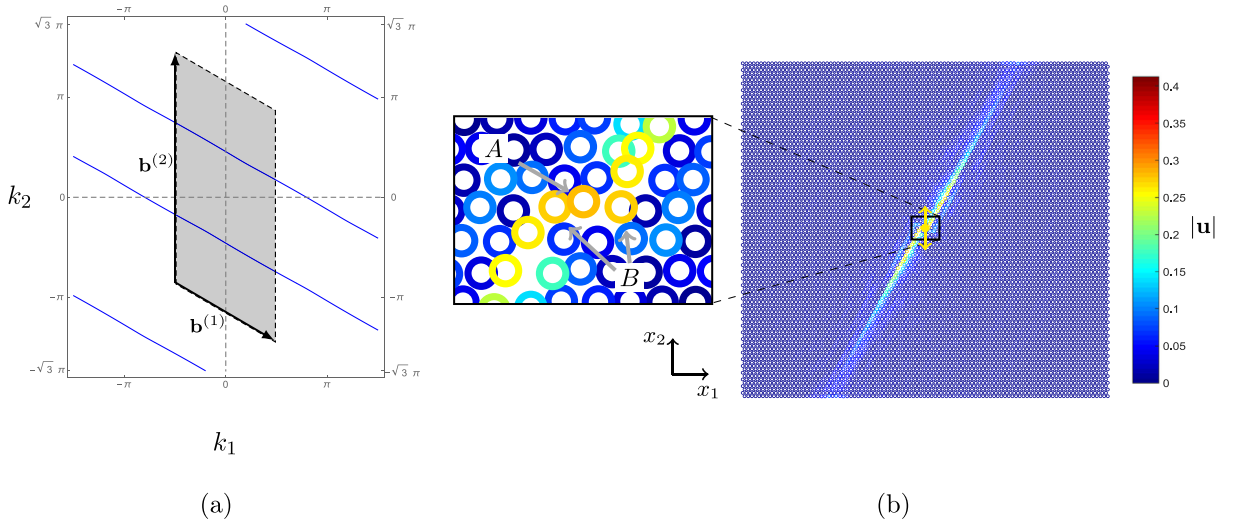
Fig. 12. (a) Slowness contours at $\Omega_G = 3$ and $\omega = 1.15\pi$ based on a modification of the results in Appendix B. The grey region represents the first Brillouin zone. (b) Transient dynamic analysis in a finite gyro-elastic lattice composed of 5000 unit cells with spinners possessing $\alpha_A = 0.8$, $\alpha_B = 0.9$ and gyricity $\Omega_G = 3$. The displacement magnitude $|\mathbf{u}|$ is given at the normalised time $t = 169.64$. The full transient solution is illustrated in Video 6 of the Supplementary Material. (For interpretation of the references to colour in this figure, the reader is referred to the web version of this article.)

Fig. 11. The system is initially at rest and the exterior lattice nodes are clamped. A wave is produced by a concentrated load, acting at the central node indicated by a yellow dot in Fig. 11; the node is of the type *A* (see Fig. 9). The applied force is $\mathbf{P}\sin(\omega t)$, where the amplitude vector $\mathbf{P} = (0, 0.96)^{\mathsf{T}}$.

In Fig. 11 the displacement magnitude $|\mathbf{u}|$ is given at time $t = 233.58$, while in the Video 5 of the Supplementary Material it is possible to see the propagation of the localised waveform during the entire numerical computation. It is evident that the wave is highly localised along the direction predicted by the dispersion properties in Fig. 10, namely perpendicular to the straight slowness contours at $\omega = 1.72\pi$.

A deeper inspection of the numerical results, evidenced by the inset on the left of Fig. 11, reveals that, while the force is applied to a node of type *A* (see Fig. 9), the wave is mainly localised in the lattice nodes of type *B*. Video 5 of the Supplementary Material shows that there is an initial stage $0 \leq t \leq 13$, in which the wave propagates from the node where the force is applied to the neighboring nodes, without an evident preferential direction. There is also a second stage where two highly localised waves are generated that depart from the two nodes of type *B* adjacent to the node where the force is applied. An additional simulation, not reported here for brevity, shows that also in the case when the force is applied to a node of type *B* the wave is highly localised along a line of nodes of this type. This is in agreement with the steady-state results reported in Carta et al. (2017a), which show that waves tend to propagate along the lines where the parameter α is larger. However, the steady-state analysis neither gives any information about the initial range when the wave moves from point *A* to point *B*, nor any indication about the wave speed, which can be estimated from the present transient simulation. In particular, the latter shows that the localised waves can be achieved in the elastic system in a relatively short finite time interval.

Next, we investigate if localised waveforms can be generated in a gyro-elastic lattice possessing uniform gyricity, but in the case $|\Omega| \neq \omega$. In this scenario, in the last terms in the right-hand sides of (37) and (38), ω is replaced by Ω_G. Fig. 12(a) shows the slowness contours for $\omega = 1.15\pi$. Once again, it can be seen that the slowness contours in Fig. 12(a) are straight lines associated with waves that propagate in the direction $(1/2, \sqrt{3}/2)$. In Fig. 12(b), the response of the system at $t = 169.64$ when subjected to the sinusoidal load $\mathbf{P}\sin(\omega t)$ is reported. There, a clear localised waveform can be observed that propagates in the direction parallel to the inclined rows of the lattice.

This response is realised in a similar way to that encountered in the previous example in Fig. 11 and Video 5. However, as evidenced by the magnification of Fig. 12(b) and Video 6, the load is able to excite more neighboring nodes, as seen in the interval $0 \leq t \leq 17$ of Video 6. As a consequence, this also leads to more than one localised wave propagating parallel to each other. These additional localised waves appear along the first and the second neighboring inclined rows to the load that contain the nodes of type *B*.

The results of Fig. 12 and Video 6 demonstrate that highly localised waves can be achieved in a gyro-elastic medium without the requirement $|\Omega| = \omega$ on the gyricity. Finally, we conclude the analysis of these waves by asking a natural question: "Can the localised waveforms be realised in a gyro-elastic lattice subjected to different initial conditions?"

To answer this question, we consider non-zero initial conditions in a neighborhood of the load. The initial conditions of the system are now modified inside a 10×10 rectangle centered at the point where the load is applied in the lattice (see Fig. 13). Each node in this region is given an initial displacement of 0.02 and an initial velocity 0.05 in the horizontal and vertical directions. All other nodes are considered to be initially at rest.
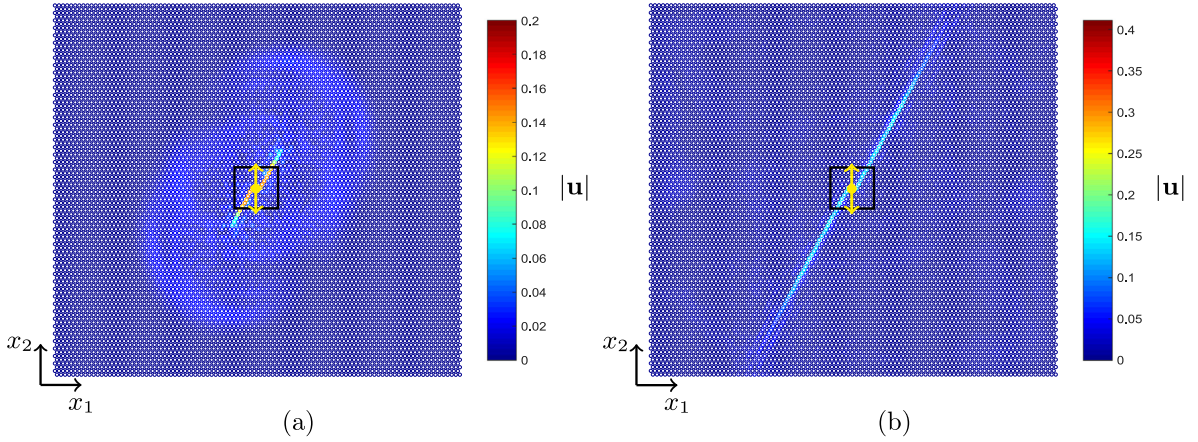
Fig. 13. Transient dynamic analysis in a finite gyro-elastic lattice subjected to non-homogeneous initial conditions within the black rectangles, centred on the position of the applied force (the yellow dots). The lattice is composed of 5000 unit cells with spinners possessing $\alpha_A = 0.8$, $\alpha_B = 0.9$ and gyricities $\Omega_A = -\Omega_B = \omega = 1.72\pi$. The displacement magnitude $|\mathbf{u}|$ is given at the normalised time (a) $t = 59.76$ and (b) $t = 233.58$. The full transient solution is illustrated in Video 7 of the Supplementary Material. (For interpretation of the references to colour in this figure, the reader is referred to the web version of this article.)

A snapshot of the lattice within the initial stage of its response is shown in Fig. 13(a). Once more, a clearly visible highly localised wave can be seen propagating along the nodes of the type *B*. Accompanying this is a vortex-type transient wave propagating outward from the load. The displacements produced by this wave are small in comparison with the dominant dynamic feature in Fig. 13(a). Hence, in this figure the maximum displacement of the color bar has been truncated to highlight this transient effect. In Fig. 13(b), the behaviour of the lattice at a much later time is shown. It is seen that the effects of the transient vortex wave are negligible and, in accordance with the slowness contours of Fig. 10(b), the highly localised waveform predicted by the dispersion analysis is achieved.

Video 7 demonstrates the effect of the non-homogeneous distribution of the initial conditions on the evolution of the system's motion. There the motion can be described in three stages. For $0 \leq t \leq 4$, the intensity of the deformations created by the non-homogeneous initial conditions within the prescribed rectangle decreases. During this time interval there are also visible deformations created by the load in its vicinity. The second stage of the lattice motion occurs for $4 \leq t \leq 25$, where the deformations created by the initial lattice configuration and the source interact. In this period, no preferential direction of the deformation is observed. The third stage takes place for $t \geq 25$, where the waveform possessing preferential directions expected from the dispersion analysis (see Fig. 10) becomes clearly visible. In this stage, nodes of the type *B* to the left and right of the load are excited and begin to generate the highly localised waveform similar to the scenario of the lattice with homogeneous initial conditions. As this happens, the influence of the initial conditions can still be seen as the vortex wave propagates outwardly from the load and interacts with the upper and lower lattice boundaries at approximately $t = 78$.

The example presented in Fig. 13 and Video 7 demonstrates that changing the initial conditions of the system will produce different transient effects but the waveforms predicted by the theoretical model of Carta et al. (2017a) in the time-harmonic regime are still realisable. We also tested the case of uniform non-homogeneous initial conditions in the whole computational domain and we obtained qualitatively the same results with the generation of a highly localised waveform.
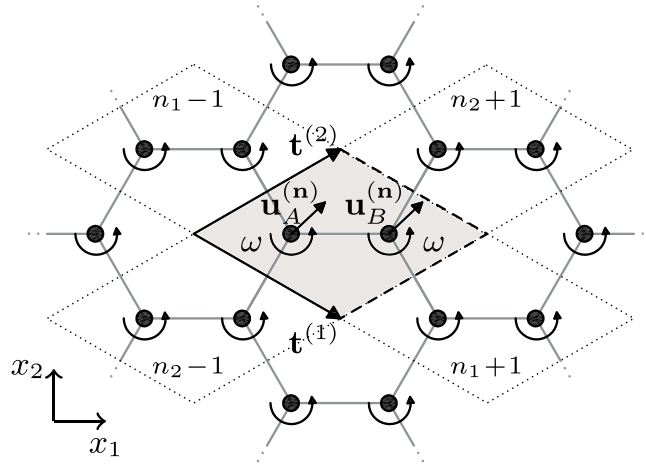
3.2. Interfacial waves in a hexagonal elastic lattice attached to gyroscopic spinners

Here, we consider a hexagonal lattice connected to an inhomogeneous array of spinners that divides the lattice into subdomains. In particular, our aim is to analyse the transient behaviour of interfacial waveforms that can appear when the boundaries between subdomains are excited at selected frequencies.

The configuration of the lattice system is shown in Fig. 14. We define the elementary cell of the lattice with the basis vectors $\mathbf{t}^{(1)} = (3/2, -\sqrt{3}/2)^{\mathrm{T}}$ and $\mathbf{t}^{(2)} = (3/2, \sqrt{3}/2)^{\mathrm{T}}$. The multi-index $\mathbf{n}$ is used again to identify the elementary cells in the lattice. In this system, the gyricity is uniform and is set equal to the radian frequency of vibration in the lattice. The displacements $\mathbf{u}_j^{(\mathbf{n})}$, $j = A, B$, of the nodes in the cell with index $\mathbf{n}$ satisfy the dynamic equations:

$$\ddot{\mathbf{u}}_A^{(\mathbf{n})} = \sum_{j=1}^{3} \mathbf{a}^{(j)} \cdot \{\mathbf{u}_B^{(\mathbf{n}-\mathbf{p}_j)} - \mathbf{u}_A^{(\mathbf{n})}\}\mathbf{a}^{(j)} - \alpha\omega\mathbf{R}\dot{\mathbf{u}}_A^{(\mathbf{n})}, \tag{40}$$

$$\ddot{\mathbf{u}}_B^{(\mathbf{n})} = \sum_{j=1}^{3} \mathbf{a}^{(j)} \cdot \{\mathbf{u}_A^{(\mathbf{n}+\mathbf{p}_j)} - \mathbf{u}_B^{(\mathbf{n})}\}\mathbf{a}^{(j)} - \alpha\omega\mathbf{R}\dot{\mathbf{u}}_B^{(\mathbf{n})}, \tag{41}$$

Fig. 14. An infinite lattice composed of elastic links connecting a periodic hexagonal array of masses. The junctions are also attached to a uniform array of gyroscopic spinners characterised by the material parameter α and having gyricity ω, which is the radian frequency of the entire system. The elementary cell is defined by the vectors $\mathbf{t}^{(1)} = (3/2, -\sqrt{3}/2)^{\mathrm{T}}$ and $\mathbf{t}^{(2)} = (3/2, \sqrt{3}/2)^{\mathrm{T}}$.
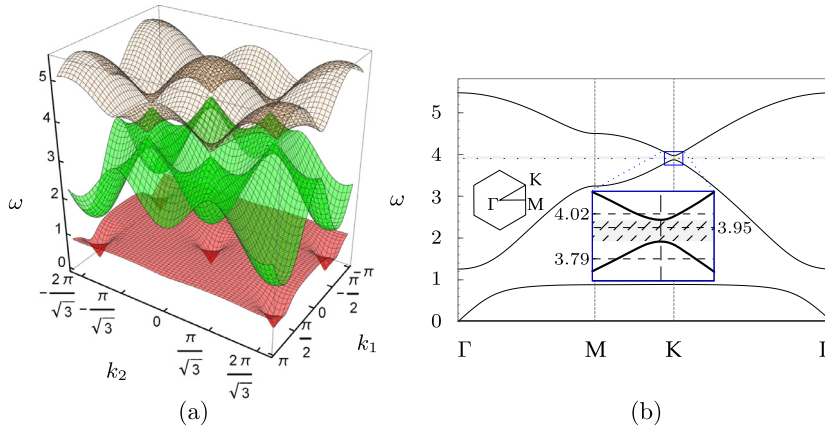
Fig. 15. Dispersion properties of the hexagonal gyro-elastic lattice of Fig. 14. (a) Dispersion surfaces and curves are given for $\alpha = 0.9$. The narrow stop band in the high-frequency regime is highlighted in the inset in part (b), which also includes the frequencies of the external excitation used in the numerical simulations. The computations are based on the results of Appendix C. (For interpretation of the references to colour in this figure, the reader is referred to the web version of this article.)

with $\mathbf{p}_1 = (0, 0)^{\mathrm{T}}$, $\mathbf{p}_2 = (1, 0)^{\mathrm{T}}$ and $\mathbf{p}_3 = (0, 1)^{\mathrm{T}}$. The last terms in the preceding right-hand sides represent the dynamic contribution of the uniform array of spinners to the lattice system.

A detailed dispersion analysis of the system was carried out in Garau et al. (2018) and is briefly reported in Appendix C. Based on this analysis, later we describe how this model is used to determine the frequencies at which interfacial waves can propagate in hexagonal systems connected to spinners with an inhomogeneous arrangement of gyricities.

3.2.1. Unidirectional interfacial waves in hexagonal chiral media with distributed gyricity

Here, we show that by using an inhomogeneous distribution of gyricities one can generate interfacial waveforms. We demonstrate how to obtain such an effect in the transient regime for the case $\alpha = 0.9$. The dispersion diagram for this value of α is shown in Fig. 15. We note that the curves admit a narrow stop band in the interval $3.685 < \omega < 3.963$. In addition, in this figure we indicate the frequencies $\omega = 3.79, 4.02$ for the harmonic excitation of the lattice, where one will encounter interfacial waves propagating in opposite directions (see Garau et al., 2018).

We consider the system shown in Fig. 16. A rectangular slab of lattice, with dimensions $100 \times 50\sqrt{3}$, is divided into two subdomains, having a zig-zag interface. The parameter $\alpha = 0.9$ and we distribute the gyricity of the spinners such that in the lower portion of the lattice $\Omega = \omega$ (nodes shown in blue in Fig. 16), while in the upper portion of the lattice $\Omega = -\omega$ (nodes shown in red in Fig. 16).

A *Matlab* code has been implemented to solve equations analogous to (40) and (41) on the 4332 nodes of the lattice in Fig. 16. The system is assumed to be initially at rest and the lattice nodes along the exterior of the slab are clamped. At the node indicated with a black dot in Fig. 17, we apply the harmonic force $\mathbf{P}\sin(\omega t)$. Here, $\mathbf{P} = 0.29 \, (1/2, \sqrt{3}/2)^{\mathrm{T}}$, so
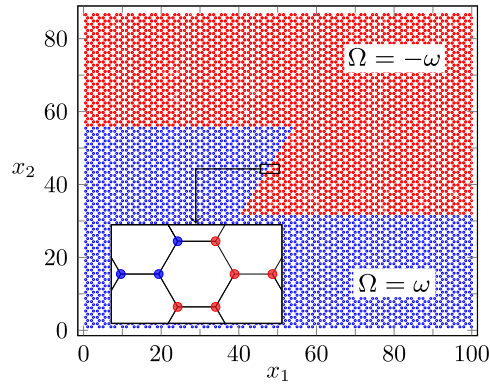
Fig. 16. Computational domain for the example of Section 3.2.1, involving a rectangular slab of a hexagonal lattice connected to gyroscopic spinners. The lattice is divided into two subdomains defined by the gyricities of the spinners, taken as $\Omega = -\omega$ ($\Omega = \omega$) for the red (blue) nodes. The parameter $\alpha = 0.9$ is uniform throughout the medium. (For interpretation of the references to colour in this figure, the reader is referred to the web version of this article.)
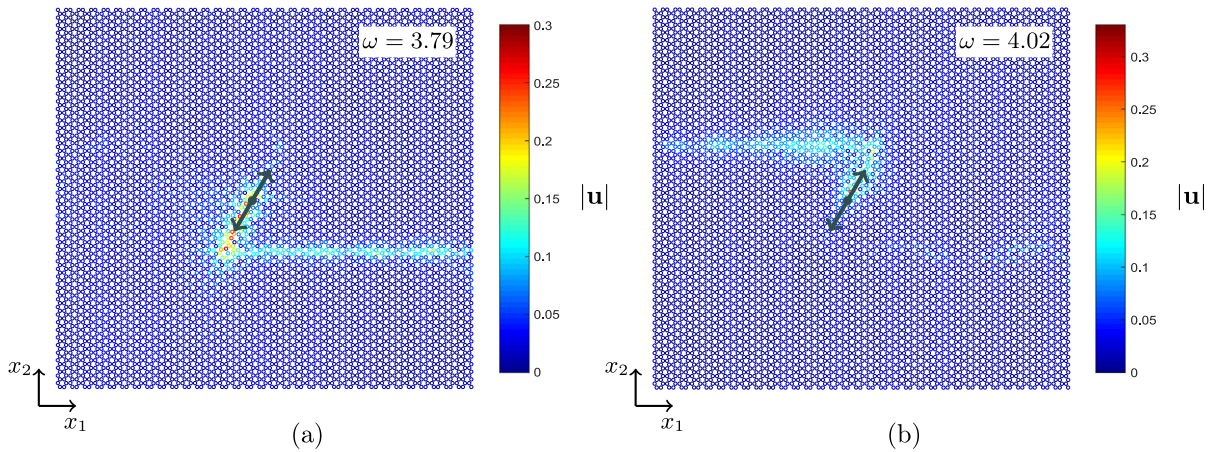
Fig. 17. Interfacial waves produced by a point force varying sinusoidally in time and applied at the interfacial node indicated with a black dot. The geometry and material details are given in Fig. 16. The displacement magnitude |**u**| is given for (a) $\omega = 3.79$, $t = 711$ and (b) $\omega = 4.02$, $t = 957$. The full transient solution is illustrated in Video 8 for the case (a) and Video 9 for the case (b) of the Supplementary Material. (For interpretation of the references to colour in this figure, the reader is referred to the web version of this article.)

that the force is aligned with the interface. The forcing frequency ω is chosen to coincide with either $\omega = 3.79$ or $\omega = 4.02$, indicated in the dispersion diagram of Fig. 15(b).

For $\omega = 3.79$ the displacement magnitude is shown in Fig. 17(a) at $t = 711$. In the figure, one can clearly see that a localised wave has appeared, that follows the internal interface to reach the right boundary of the domain.

In Fig. 17(b), the displacement magnitude is shown for $\omega = 4.02$ at $t = 957$. The wave propagates along the interface, but in the direction opposite to that in Fig. 17(a). The transient analysis shows a different speed of propagation of the two interfacial waves at the frequencies $\omega = 3.79$ and $\omega = 4.02$, where the speed of propagation is higher in the first case.

As a further illustration, in Videos 8 and 9 of the Supplementary Material we show the results of the transient simulations during the entire motion, for the two cases analysed in Fig. 17(a) and (b), respectively. The videos show some common features and differences. As in the previous example of Section 3.1.1, initially the wave propagates from the forced node to the neighboring ones without an evident preferential direction, before developing localised patterns in a finite and relatively short time-interval. For $\omega = 3.79$, the interfacial wave propagates downwards from the beginning along the inclined part of the lattice interface, while for $\omega = 4.02$ initially the wave propagates in both directions and after this initial period only upward.

In both cases, the wave slows down when it reaches one of the corners in the zig-zag interface. As the wavefront tries to pass through the corner, it produces some scattering into the bulk of the lattice, which is also evidenced by the lower amplitude of the displacement in the horizontal part of the interface.

It is worth mentioning that the effects shown here are independent of the position of the load. In Fig. 2 we show the displacement amplitude when the load is applied on the upper horizontal edge of the interface. In particular, we considered a harmonic force $\mathbf{P}\sin(\omega t)$, with $\mathbf{P} = 0.29\,(1, 0)^\mathrm{T}$ and $\omega = 3.79$, applied at the node indicated with a black dot in the figure.
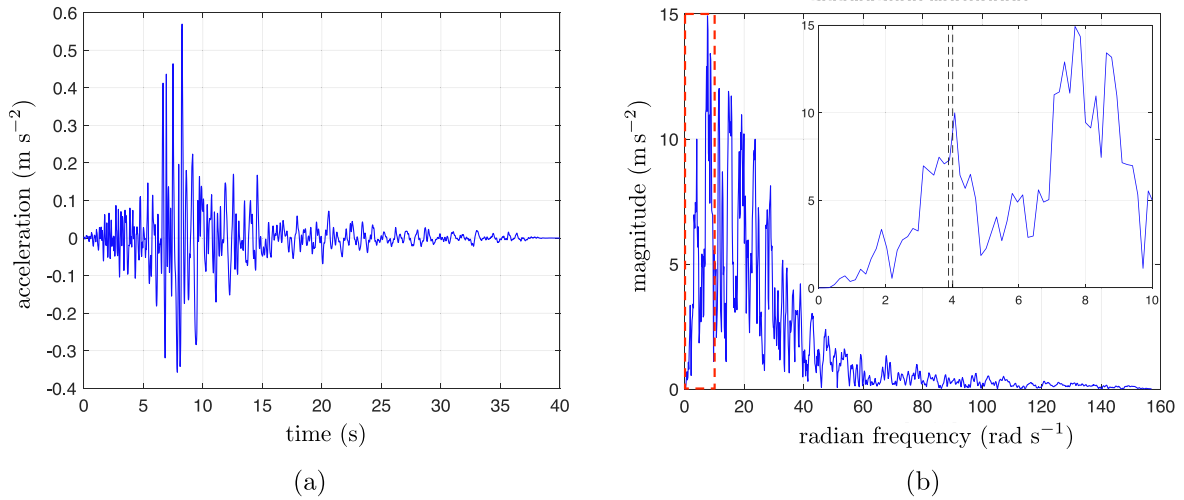
Fig. 18. (a) Accelerations produced by the accelerogram NORTHR_ORR090.AT2 as a function of time. (b) The Fast Fourier Transform of the data in (a); a magnification of the magnitude of frequency spectrum in the frequency interval [0,10] (highlighted by the red dashed box) is presented in the inset of the figure. There, the frequencies 3.82 and 4.02, corresponding to the interfacial wave frequencies of Fig. 16, are shown by vertical dashed black lines. (For interpretation of the references to colour in this figure, the reader is referred to the web version of this article.)

As for the case in Fig. 17(a), the interfacial wave propagates to the right of the load and, after passing the two corners, towards the right boundary of the lattice slab. The generation and propagation of the interfacial waves for this case can be observed in the Video 2 of the Supplementary Material.

Finally, we investigate the response of the inhomogeneous gyro-elastic medium when subjected to a transient load along the interface. In what follows, we consider a gyro-elastic lattice with $cLm^{-1} = 1\mathrm{m\ s^{-2}}$ and $L = \gamma^{-1}$ m. In this way, the magnitude of the loading and the radian frequency of the structure in the physical and dimensionless settings coincide.

The load is chosen to represent the acceleration history measured by an accelerogram (labelled NORTHR_ORR090.AT2) that recorded the famous seismic event in Northridge, 1994. The data for this event was captured within a 40 s period. The real signal is shown in Fig. 18(a). For the simulation below we have implemented a load that repeats the signal generated by this earthquake after every 40 time units.

In Fig. 18(b) the frequency spectrum (in rad s^{-1}) obtained using the Fast Fourier Transform of the signal data is given. The last result shows that the load is the superposition of multiple frequency components, with the largest amplitudes in the frequency interval [0,30], which includes some of the pass bands of the lattice structure, reported in Fig. 15. Hence, we may anticipate multiple harmonic wave components to be excited by such a load.

As in the examples of Fig. 17, we apply the load along the zig-zag interface at the node indicated at the black dot in Fig. 19, and this acts parallel to the inclined part of the internal boundary. Fig. 19 shows the behaviour of the inhomogeneous gyro-elastic lattice at $t = 757.49$. While less localised than in the examples shown in Fig. 17, a propagating interfacial wave is still clearly visible. In particular, the most prominent dynamic feature that can be observed is an interfacial wave that propagates to the right-hand boundary of the lattice. There is also some evidence of an interfacial wave that attempts to move along the interface in the opposite direction, but has not reached the left lattice boundary of the computational domain at the end of the analysis. One possible explanation for this is based on the results of Fig. 17, associated with the harmonic excitation of the gyro-elastic lattice. There, it was revealed that the interfacial wave travels faster to the right boundary.

Video 10 of the Supplementary Material shows how the behaviour of the lattice evolves in time as a result of the load with multiple frequency content. As expected, it can be seen that many waves are created by the load that propagate in multiple directions within the time interval $0 \leq t \leq 250$. Following this interval, these processes are accompanied by an interfacial wave that begins to propagate downward along the interface in the lattice from the load. The propagation of the interfacial wave is not as clear as in the example of Fig. 17, due to the wave radiation produced by the source. There is a region in the vicinity of the load where the deformations in each direction of the lattice are comparable. This occurs until $t = 350$ and following this the interfacial wave can be clearly seen to propagate towards the right-hand boundary of the lattice.

The example presented in Fig. 19 and Video 10 indicates that multiple waves can be generated by a transient source, including waveforms occurring at special frequencies. The frequency spectrum of the load chosen here contains information about such frequencies, but they are not the dominant frequencies composing the signal (see inset of Fig. 18(b)). Nevertheless, here we have shown that the interfacial waveforms obtained at selected frequencies are still realisable and represent a significant dynamic effect in transient loading configurations.
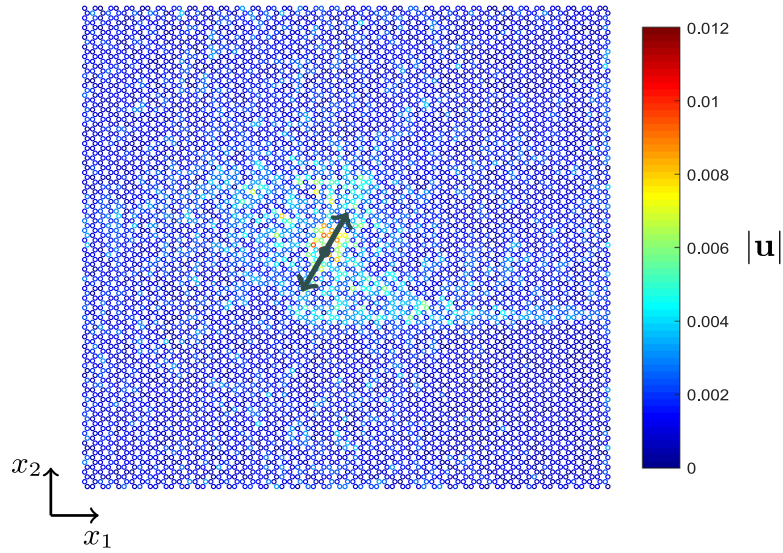
Fig. 19. Response of an inhomogeneous gyro-elastic lattice with a zig-zag interface subjected to transient loading. The geometry and material details are given in Fig. 16. The displacement magnitude |**u**| is given for $t = 757.49$. The full transient solution is illustrated in Video 10 of the Supplementary Material. (For interpretation of the references to colour in this figure, the reader is referred to the web version of this article.)

4. Advanced applications

In this section, we give some further illustrations showing that the hexagonal gyro-elastic lattice model analysed in Section 3.2 can be used to design structured devices with wave-guiding properties having applications in topological protection and cloaking.

4.1. Topological protection

Here, we investigate the capability of the gyro-elastic lattice in supporting edge waves. To this end, we perform the transient analysis of a gyro-elastic hexagonal lattice arranged as in Fig. 20, containing a hexagonal cavity. The unit cell of the gyro-elastic lattice is as in Fig. 14.
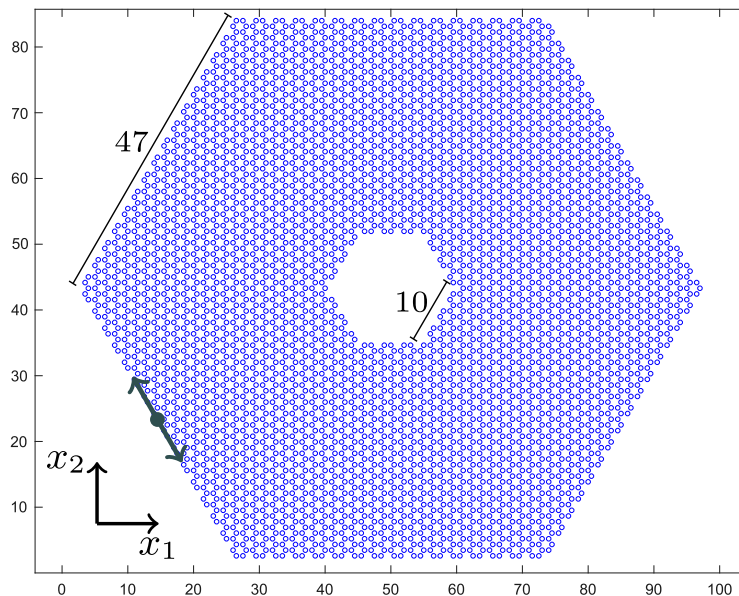
Fig. 20. Geometry of the domain analysed in Section 4.1. The parameters of the gyroscopic spinners are $\Omega = \omega = 3.95$ and $\alpha = 0.9$. (For interpretation of the references to colour in this figure, the reader is referred to the web version of this article.)

The gyricity and parameters characterising the motion and type of the spinners are uniform and taken as $\Omega = \omega$ and $\alpha = 0.9$, respectively. The lattice is assumed to be at rest initially and it is excited on the external boundary at the point indicated by the dot in Fig. 20 with the sinusoidal force $\mathbf{P}\sin(\omega t)$. In this case, $\mathbf{P} = A(1/2, -\sqrt{3}/2)^{\mathsf{T}}$, with $A = 7.7 \times 10^{-2}$ and $\omega = 3.95$. This frequency is within the narrow high-frequency stop band indicated in Fig. 15.

Video 11 shows that the external force generates a wave that propagates along the external boundary of the domain in the clockwise direction. Some snapshots of this video are presented in Fig. 21 at various times of the computation. This displacement is ten times larger than the maximum displacement inside the rest of the system and the displacement is concentrated near the external boundary of the lattice. In order to better visualise the displacement field in the whole domain, in Video 11 and Fig. 21 we have truncated the total displacement scale at $|\mathbf{u}| = 0.1$. In the bulk of the lattice, and in particular on the internal hexagonal boundary, the displacements are negligibly small with respect to the values attained on the external hexagonal boundary. Accordingly, an object placed in the cavity of the domain would be protected from any dynamic disturbance produced outside the lattice for the considered loading.

Video 12 shows a magnified view of the lattice near the point of application of the external force. The masses rotate in the plane in the anti-clockwise direction, yet the edge wave propagates along the exterior boundary in the clockwise direction. This counter-intuitive phenomenon is typical with wave motion in discrete gyro-elastic media.

4.2. Cloaking

In the final example considered in this paper, we show that one can design a structured gyro-elastic medium that can act as an efficient cloaking device to hide a defect in a discrete lattice (see Fig. 22(a)). The cloak possesses an inner and outer hexagonal annulus, each of which is split into two domains, as shown in Fig. 22(b). Throughout the cloak the quantity $\alpha|\Omega|$, characterising the magnitude of the effective input of the gyroscopes to the cloak, is uniform. The value of $\alpha\Omega$ in each subdomain of the cloak is indicated in Fig. 22(b).

We remark that the design of the cloaking device is similar to that proposed in Brun et al. (2012). However, here we are considering a discrete medium, while in Brun et al. (2012) a homogenised continuum was implemented in the design and simulations.

We consider a rectangular slab of hexagonal lattice with dimensions $241.5 \times 199\sqrt{3}/2$. We study the dynamic response of this lattice in three scenarios: (i) when there is no defect and hence the lattice is homogeneous; (ii) when the lattice contains a defect, represented by the black hexagon in Fig. 22(a) and (b); (iii) when the defect is coated by the gyro-elastic cloak, marked in red and blue in Fig. 22(a) and (b). As demonstrated below, without the cloak the defect would create noticeable effects, such as scattering and shielding, when interacting with waves propagating in the ambient medium. Conversely, when the cloak designed as in Fig. 22(b) is inserted, these effects are reduced, especially in particular directions, reconstructing the wave pattern as if the defect were not present.

In all the computations presented here, the lattice is assumed to be initially at rest. Perfectly Matched Layers (PML) are used to minimise the reflections produced at the edges of the lattice. Elastic waves are generated by an applied displacement, indicated by a black arrow in Fig. 22(a). The imposed displacement is positioned at $(75, 50\sqrt{3})$ (represented by the black dot in Fig. 22(a)) and is expressed by $\mathbf{Q}\sin(\omega t)$, where $\mathbf{Q} = (0.5, 0)^{\mathsf{T}}$ and $\omega = 0.3$. We note that the chosen value of the frequency ω is relatively low.

We start by considering the case (i), when the lattice is homogeneous. Video 13 of the Supplementary Material shows the response of the medium to the external excitation. Waves with a circular front propagate outward from the applied displacement and shadow regions can be observed in the vertical directions relative to the excitation. As expected, due to the hexagonal lattice microstructure, the wave field is not radially symmetric. Additionally, we observe that the waves propagating in the lattice are not affected by their interactions with the boundary due to the presence of the PML. The displacement field in the lattice taken at a large time instant is illustrated in Fig. 23(a).

Next, we consider the case (ii) when a defect is situated in the lattice. The defect is represented by a region of nodes that are connected to each other by links stiffer than those in the ambient medium. The region of the defect, indicated by the black hexagon in Fig. 22(b), has side length equal to 7.

Fig. 23 (b) shows the response of the system for a large value of time. A clear shadow can be seen to the right of the defect, in addition to other shadows created in the vertical direction. Furthermore, there are scattered waves produced by the left-most vertex of the defect that propagate at $\pm 60°$ and $\pm 90°$ to the positive horizontal direction relative to this vertex.

Video 14 in the Supplementary Material shows how the displacement field in Fig. 23(b) is achieved. The outgoing waves from the applied displacement reach the defect at $t = 36$. Until this time, the wave pattern is similar to the field produced in the homogeneous lattice. After $t = 36$, the left-most vertex of the defect also begins to act as a source, creating scattered waves that interact with the waves generated by the imposed displacement. In addition, the shadow regions described in Fig. 23(b) take form after $t = 36$.

Fig. 23 (c) shows the response of the system for the case (iii) when the defect is coated by the gyro-elastic cloak shown in Fig. 22(b). In particular, we notice that the coating is capable of reconstructing the wave pattern to the right of the defect. As can be seen from Fig. 23(c), the cloak acts like a resonator, keeping the displacements in the defect region very small. Accordingly, the gyroscopic spinners inside the cloak re-route the incoming waves around the defect, leaving the cloak interior almost disturbed. The resulting wave pattern to the right of the cloaked defect is in good agreement with the pattern
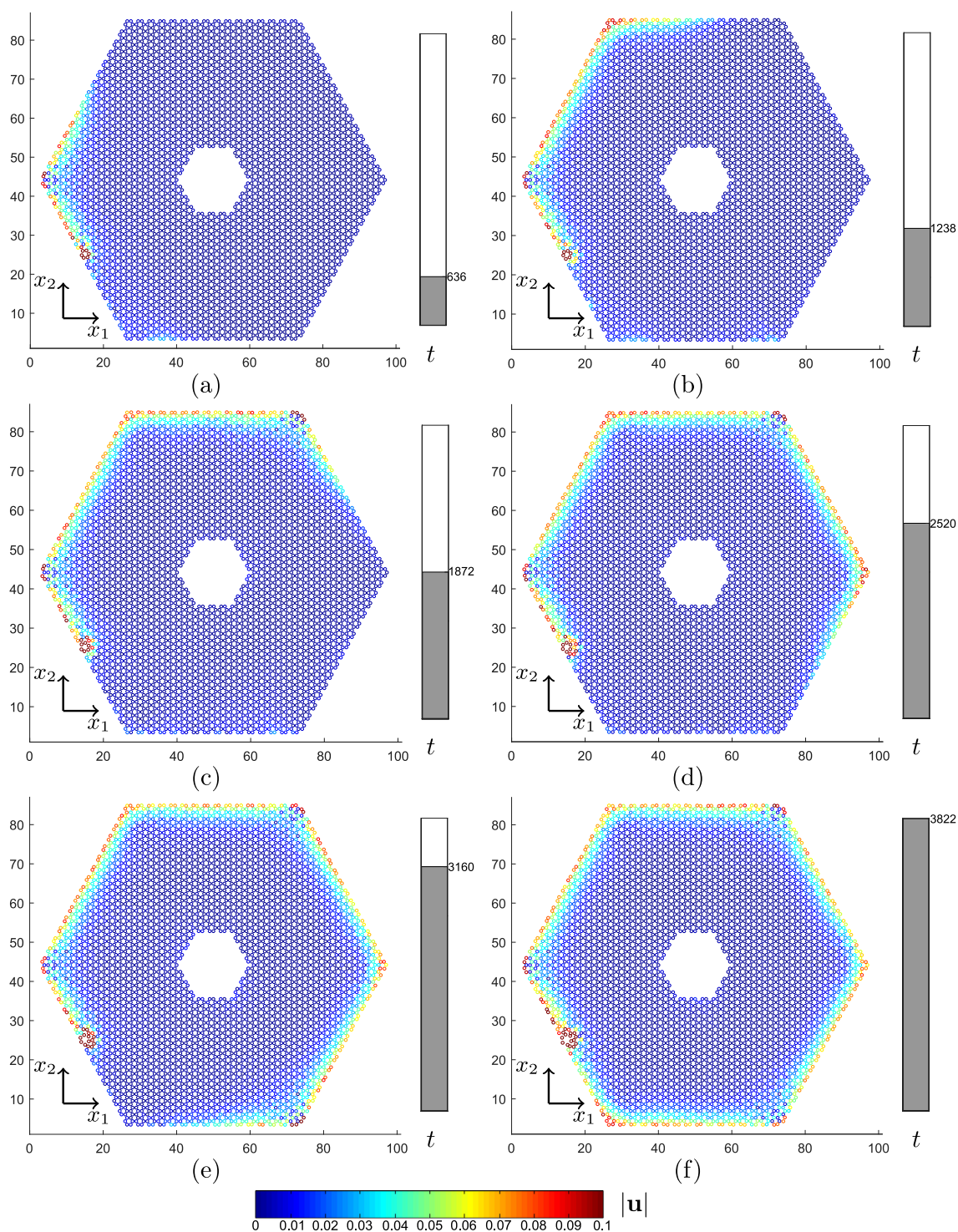
**Fig. 21.** A selection of snapshots from the numerical computation shown in Video 11 that illustrates the response of the gyro-elastic lattice excited on the external boundary. The displacement magnitude |**u**| is given at times t indicated on the bar on the right of each figure. (For interpretation of the references to colour in this figure, the reader is referred to the web version of this article.)
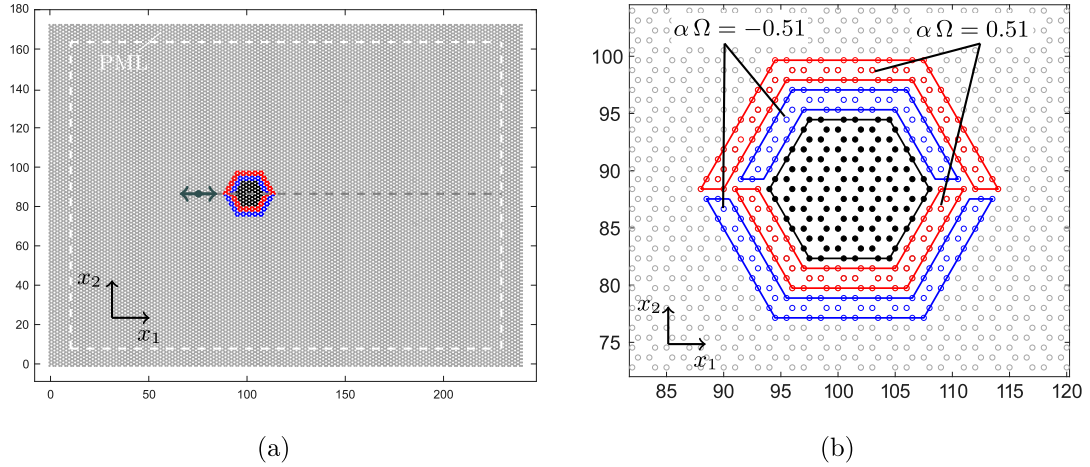
Fig. 22. (a) A hexagonal lattice containing a defect (black hexagonal region), coated by a gyro-elastic cloak (red and blue regions). Along the exterior boundary of the lattice Perfectly Matched Layers are used, whose interior boundary is represented by a white dashed line. The position of the external excitation is indicated by a black arrow. (b) A magnification of the cloaked defect. The region bounded by the red (blue) lines contains lattice nodes connected to gyroscopic spinners with $\alpha\Omega = 0.51$ ($\alpha\Omega = -0.51$). The defect is represented by the black dots, connected by links of stiffness equal to 12, whereas in the ambient medium the link stiffness is equal to unity. (For interpretation of the references to colour in this figure, the reader is referred to the web version of this article.)
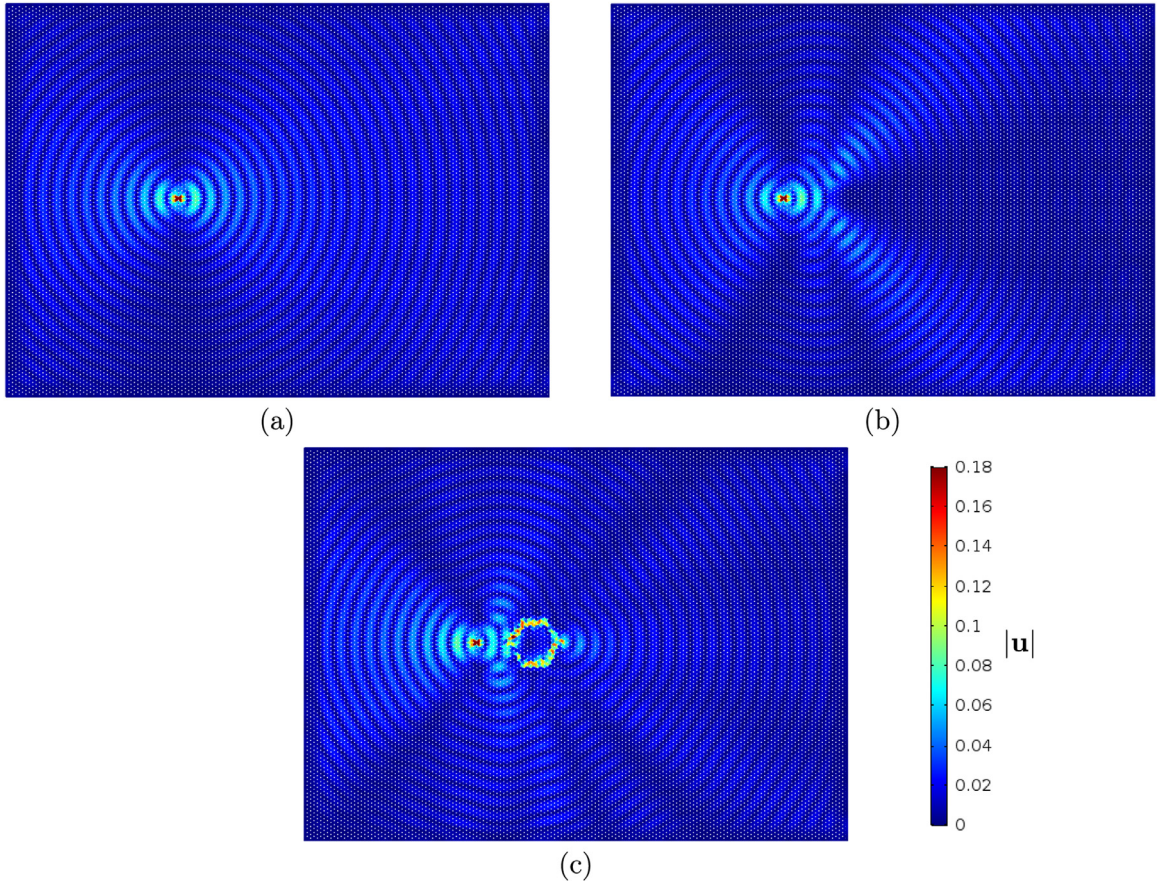
Fig. 23. The displacement field produced by a point excitation when the hexagonal lattice (a) is homogeneous, (b) contains the defect and (c) contains the defect that is coated by the gyro-elastic cloak (see Fig. 22). The figures show the responses of the lattices at $t = 1353$. (For interpretation of the references to colour in this figure, the reader is referred to the web version of this article.)
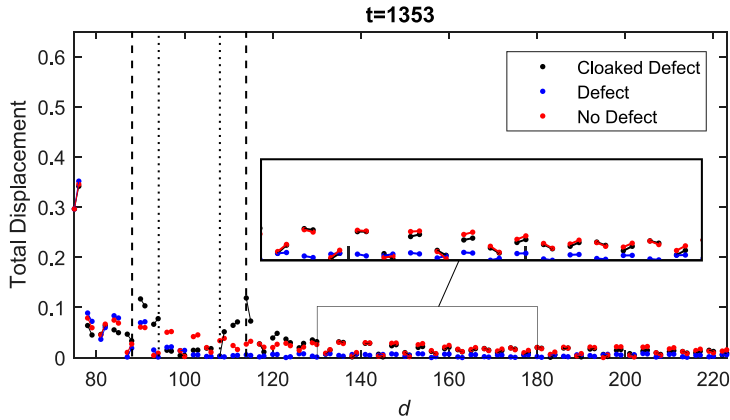
Fig. 24. Total displacement of the hexagonal lattice subjected to a harmonic excitation, computed along the grey dashed line shown in Fig. 22, for the case when the structure (i) is homogeneous, (ii) contains the defect and (iii) contains the defect that is coated by the gyro-elastic cloak (see Fig. 22). The location of the defect along this line is indicated by the vertical dotted lines and the gyro-elastic cloak is contained in the region between the dashed and dotted lines. A magnification of the results obtained for $130 \leq d \leq 180$ is also presented for the sake of comparison. (For interpretation of the references to colour in this figure, the reader is referred to the web version of this article.).

in Fig. 23(a) for the case without any inhomogeneity. We also note that there exist narrow regions in oblique directions where the cloaking device is less efficient in reconstructing the wave field obtained in the case of the homogeneous lattice.

In Video 15 we show the results of the transient analysis for the lattice with the coated defect. Until $t = 26$, the displacement pattern of the system is similar to that of the homogeneous lattice. After this instant, waves begin to interact with the gyro-elastic cloak. For $26 < t < 93$, we see scattering due to the left-most vertex of the cloak in the vertical directions and waves being re-routed through the coating around the defect. In this time interval, the displacements in the defect are visibly small. After $t = 93$, the right-most vertices of the cloak begin to act as sources, producing elastic waves with circular fronts propagating away from the cloak in several directions. These waves lead to a visibly excellent reconstruction of the wave pattern observed in the homogeneous medium to the right of the cloak. It is noted that as this reconstruction occurs, the gyro-elastic medium undergoes displacements with larger amplitudes in comparison to the behaviour of the far-field generated in the ambient lattice by the source.

In order to illustrate the efficiency of the cloak quantitatively, we determine the total displacements of the lattice nodes for a given time and along the horizontal dashed grey line shown in Fig. 22(a). Along this line, the distance between two lattice nodes is alternatively equal to one or two lattice units. The total displacements along this line are calculated for all three computations presented in Fig. 23 and they are plotted in Fig. 24. The results for the case of the lattice with the defect show a significant reduction in the amplitude of the displacement field to the right of the defect, when compared with the results of the homogeneous lattice. On the other hand, the introduction of the cloak allows for a good reconstruction of the displacement field to the right of the cloak, to the extent that in some regions the results for the coated defect and the homogeneous case are indistinguishable. In scenario (iii), we also note larger displacements in the gyro-elastic cloak, which re-routes the external waves around the defect, and very small displacements in the defect region.

Video 16 shows how the displacement profiles in the three scenarios change with time. The video reveals that it takes 438 time units for the cloak to approximately reproduce the displacement field in the homogeneous lattice. After $t = 438$, in the region to the right of the cloak, the total displacements for the cases of the cloaked defect and the homogeneous lattice agree very well and move together in phase.

Finally, we recall that in the illustrations of Fig. 23 and Video 15, the quantity $\alpha|\Omega|$, within the gyro-elastic cloak, is uniform. We remark that the proposed design in Fig. 22 corresponds to a wide class of arrays of gyroscopes, with uniform distributions of the gyricity magnitude $|\Omega|$ and physical properties characterised by α, for which the cloaking effect identified here is achievable.

5. Conclusions

We have developed a new asymptotic model that describes the transient motion of a mass connected to a gyroscopic spinner and to a truss system of elastic rods. For this gyro-elastic structure, we have derived a linearised model using the assumption that the nutation angle of the spinner is a small quantity. For simple configurations, we have obtained an analytical solution, that is in excellent agreement with the numerical results based on the finite element method, despite the fact that the dimensionality of the two models is different.

We have extended this study to the dynamic analysis of an elastic lattice attached to a system of gyroscopic spinners, focussing on special dynamic regimes possessed by the medium and previously identified in Carta et al. (2017a) and Garau et al. (2018) under time-harmonic conditions. Specifically, we have shown how highly localised waveforms and unidirectional interfacial waves are generated and propagate through a gyro-elastic lattice in the transient regime.

We have demonstrated that these dynamic effects can be obtained for different initial conditions and under an exciting load with broadband frequency content such as the recorded accelerogram of a real seismic event.

We have also developed two important applications of a gyro-elastic system. The first one shows that a gyro-elastic medium can be used to construct a robust topological insulator that, when excited on the exterior boundary at a given frequency, is capable of confining the waves to this boundary, leaving the interior of the structure almost undisturbed. The second application concerns the design of a structured gyro-elastic cloak, that can be efficiently used to hide the presence of a defect in the discrete medium, preventing the defect from having significant interactions with external excitations. We envisage that the models proposed in this paper will be very useful in seismic protection and civil engineering, where systems capable of controlling or suppressing the effects of unwanted vibrations are of great importance.

Acknowledgments

Appendix A. Angular momentum balance of the gyroscopic spinner

The derivation of the equations of motion (3) of the gyroscopic spinner are presented here (see also Carta et al., 2018; Goldstein et al., 2001; Nieves et al., 2018). The generalised coordinates or Euler angles are the precession ϕ, the nutation θ and the spin ψ angles (see Fig. 3(b)).

We introduce both a fixed frame of reference $\mathcal{F}$, with basis $\{\mathbf{e}_1, \mathbf{e}_2, \mathbf{e}_3\}$ and coordinate system $Ox_1x_2x_3$, and a moving frame of reference $\mathcal{F}'$, which follows the gyroscopic spinner as it precesses and nutates (but not as it spins). The moving frame $\mathcal{F}'$ has basis $\{\mathbf{e}_1', \mathbf{e}_2', \mathbf{e}_3'\}$ (which is time-dependent) and coordinate system $Ox_1'x_2'x_3'$. The basis in the moving frame can be written via the basis $\{\mathbf{e}_1, \mathbf{e}_2, \mathbf{e}_3\}$ in the fixed frame as

$$\begin{aligned}
\mathbf{e}_1' &= \cos(\phi(t))\mathbf{e}_1 + \sin(\phi(t))\mathbf{e}_2, \\
\mathbf{e}_2' &= -\cos(\theta(t))\sin(\phi(t))\mathbf{e}_1 + \cos(\theta(t))\cos(\phi(t))\mathbf{e}_2 + \sin(\theta(t))\mathbf{e}_3, \\
\mathbf{e}_3' &= \sin(\theta(t))\sin(\phi(t))\mathbf{e}_1 - \sin(\theta(t))\cos(\phi(t))\mathbf{e}_2 + \cos(\theta(t))\mathbf{e}_3 .
\end{aligned} \tag{A.1}$$

Starting from the angular momentum balance (1), we express the angular velocity of the gyroscopic spinner $\boldsymbol{\omega}_g$ as

$$\boldsymbol{\omega}_g = \boldsymbol{\omega}_{\mathcal{F}'\mathcal{F}} + \dot{\psi}\,\mathbf{e}_3', \tag{A.2}$$

where the dot denotes differentiation with respect to time. Here, $\boldsymbol{\omega}_{\mathcal{F}'\mathcal{F}}$ is the angular velocity of the basis in $\mathcal{F}'$ relative to the basis in $\mathcal{F}$ and the last term in the right-hand side corresponds to the angular velocity of the spinner about the local axis Ox_3' in $\mathcal{F}'$. The angular velocity $\boldsymbol{\omega}_{\mathcal{F}'\mathcal{F}}$ can be written in terms of the Euler angles as

$$\boldsymbol{\omega}_{\mathcal{F}'\mathcal{F}} = \dot{\theta}\mathbf{e}_1' + \dot{\phi}\sin(\theta)\mathbf{e}_2' + \dot{\phi}\cos(\theta)\mathbf{e}_3' . \tag{A.3}$$

Taking into account that

$$\dot{\mathbf{e}}_j' = \boldsymbol{\omega}_{\mathcal{F}'\mathcal{F}} \times \mathbf{e}_j', \tag{A.4}$$

the angular momentum balance (1) takes the form

$$\mathbf{M}_e = \mathbf{I}_g \mathcal{A}_g + \boldsymbol{\omega}_{\mathcal{F}'\mathcal{F}} \times \mathbf{I}_g \boldsymbol{\omega}_g . \tag{A.5}$$

In the above,

$$\mathcal{A}_g = \ddot{\theta}\mathbf{e}_1' + (\ddot{\phi}\sin(\theta) + \dot{\phi}\dot{\theta}\cos(\theta))\mathbf{e}_2' + (\ddot{\phi}\cos(\theta) - \dot{\phi}\dot{\theta}\sin(\theta) + \ddot{\psi})\mathbf{e}_3' \tag{A.6}$$

is the angular acceleration in the rotating frame of reference.

The explicit components of (A.5) are

$$\begin{aligned}
M_1' &= I_0\ddot{\theta} + \dot{\phi}\sin(\theta)[-I_0\dot{\phi}\cos(\theta) + I_1(\dot{\phi}\cos(\theta) + \dot{\psi})], \\
M_2' &= I_0[\ddot{\phi}\sin(\theta) + 2\dot{\theta}\dot{\phi}\cos(\theta)] - I_1\dot{\theta}(\dot{\phi}\cos(\theta) + \dot{\psi}), \\
M_3' &= I_1(\ddot{\psi} + \ddot{\phi}\cos(\theta) - \dot{\phi}\dot{\theta}\sin(\theta)),
\end{aligned} \tag{A.7}$$

where M_j', $1 \leq j \leq 3$, are the components of the external moment vector $\mathbf{M}_e$ when written in terms of the basis $\{\mathbf{e}_1', \mathbf{e}_2', \mathbf{e}_3'\}$.

We denote by M_j, $1 \leq j \leq 3$, the components of the external moment vector $\mathbf{M}_e$ when interpreted in terms of the basis of the fixed frame $\mathcal{F}$. From (A.1), we have

$$\begin{pmatrix} M_1 \\ M_2 \\ M_3 \end{pmatrix} = \begin{pmatrix} \cos(\phi) & -\cos(\theta)\sin(\phi) & \sin(\theta)\sin(\phi) \\ \sin(\phi) & \cos(\theta)\cos(\phi) & -\sin(\theta)\cos(\phi) \\ 0 & \sin(\theta) & \cos(\theta) \end{pmatrix} \begin{pmatrix} M'_1 \\ M'_2 \\ M'_3 \end{pmatrix}. \tag{A.8}$$

Finally, from (A.7) and (A.8) the components of the external moment (3) in the fixed coordinate system are derived.

Appendix B. Dispersion relation for the triangular lattice

Here the dispersion relation for the triangular lattice of Fig. 9 is derived, following the analytical treatment described in Carta et al. (2017a). To identify waves in the lattice, one can look for the solutions in the form

$$\mathbf{u}_j^{(\mathbf{n})} = \mathbf{U}_j^{(\mathbf{n})} e^{i\omega t}, \quad j = A, B. \tag{B.1}$$

The amplitudes $\mathbf{U}_j^{(\mathbf{n})}$, $j = A, B$, satisfy the Bloch-Floquet conditions

$$\mathbf{U}_j^{(\mathbf{n}+\mathbf{a})} = \mathbf{U}_j^{(\mathbf{n})} e^{i\mathbf{k}\cdot\mathbf{Ta}}, \qquad \mathbf{T} = [\mathbf{t}^{(1)}, \mathbf{t}^{(2)}] = \begin{pmatrix} 2 & \frac{1}{2} \\ 0 & \frac{\sqrt{3}}{2} \end{pmatrix}, \tag{B.2}$$

where $\mathbf{k} = (k_1, k_2)^\mathsf{T}$ is the Bloch or wave vector. Combining this with (37) and (38), we retrieve the dispersion relation

$$\det[\mathbf{C} - \omega^2 (\mathbf{I}_4 - \mathbf{S})] = 0, \tag{B.3}$$

where $\mathbf{I}_4$ is the 4×4 identity matrix and the matrix characterising the effect of the spinners is

$$\mathbf{S} = i\, \mathrm{diag}(\alpha_A \mathbf{R}, -\alpha_B \mathbf{R}).$$

In addition, in (B.3) the stiffness matrix $\mathbf{C}$ is given by

$$\mathbf{C} = \begin{pmatrix} \mathbf{C}^{(1)} & \mathbf{C}^{(2)} \\ \mathbf{C}^{(2)} & \mathbf{C}^{(1)} \end{pmatrix},$$

where

$$\mathbf{C}^{(1)} = \begin{pmatrix} 3 - \frac{1}{2}\cos(\zeta) & -\frac{\sqrt{3}}{2}\cos(\zeta) \\ -\frac{\sqrt{3}}{2}\cos(\zeta) & 3\left(1 - \frac{1}{2}\cos(\zeta)\right) \end{pmatrix}$$

and

$$\mathbf{C}^{(2)} = \begin{pmatrix} -e^{-i(\zeta+\xi)}\left(2\cos(\zeta+\xi) + \frac{1}{2}\cos(\xi)\right) & \frac{\sqrt{3}}{2}e^{-i(\zeta+\xi)}\cos(\xi) \\ \frac{\sqrt{3}}{2}e^{-i(\zeta+\xi)}\cos(\xi) & -\frac{3}{2}e^{-i(\zeta+\xi)}\cos(\xi) \end{pmatrix},$$

with $\xi = \frac{k_1}{2} - \frac{\sqrt{3}k_2}{2}$ and $\zeta = \frac{k_1}{2} + \frac{\sqrt{3}k_2}{2}$.

Appendix C. Dispersion relation for the hexagonal lattice

Waves propagating in the hexagonal medium of Fig. 14 can be identified by substituting into (40) and (41) solutions of the form (B.1) satisfying (B.2), where the matrix $\mathbf{T}$ is now

$$\mathbf{T} = \begin{pmatrix} \frac{3}{2} & \frac{3}{2} \\ -\frac{\sqrt{3}}{2} & \frac{\sqrt{3}}{2} \end{pmatrix}. \tag{C.1}$$

The eigenfrequencies of the hexagonal gyroscopic system can be obtained from Eq. (B.3), with the following definitions of the stiffness matrix

$$\mathbf{C} = \begin{pmatrix} \frac{3}{2} & 0 & -1 - \dfrac{e^{-i\eta} + e^{-i\sigma}}{4} & \dfrac{\sqrt{3}(e^{-i\eta} - e^{-i\sigma})}{4} \\ 0 & \frac{3}{2} & \dfrac{\sqrt{3}(e^{-i\eta} - e^{-i\sigma})}{4} & -\dfrac{3(e^{-i\eta} + e^{-i\sigma})}{4} \\ -1 - \dfrac{e^{i\eta} + e^{i\sigma}}{4} & \dfrac{\sqrt{3}(e^{i\eta} - e^{i\sigma})}{4} & \frac{3}{2} & 0 \\ \dfrac{\sqrt{3}(e^{i\eta} - e^{i\sigma})}{4} & -\dfrac{3(e^{i\eta} + e^{i\sigma})}{4} & 0 & \frac{3}{2} \end{pmatrix} \tag{C.2}$$
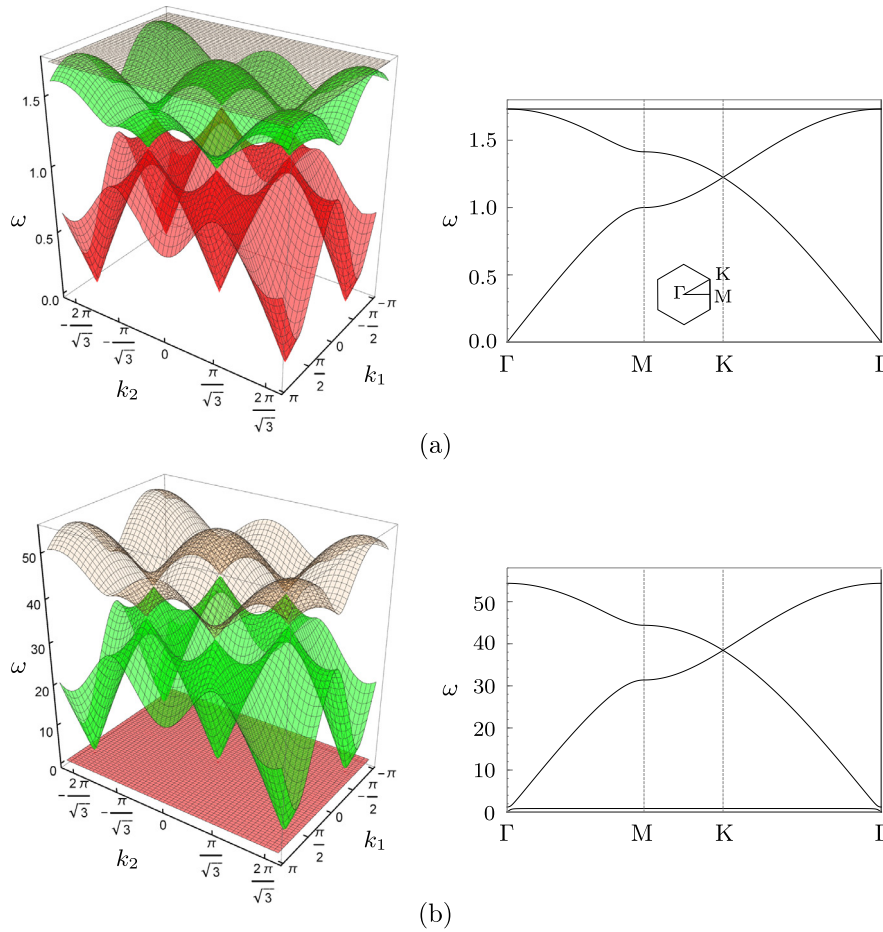
Fig. 25. Dispersion properties of the hexagonal gyro-elastic lattice of Fig. 14. (a) $\alpha = 0$, (b) $\alpha = 0.9999$. The computations are based on the dispersion relation (B.3), with (C.2) and (C.3). (For interpretation of the references to colour in this figure, the reader is referred to the web version of this article.)

with $\eta = (3k_1 - \sqrt{3}k_2)/2$ and $\sigma = (3k_1 + \sqrt{3}k_2)/2$, and the gyroscopic matrix

$$\mathbf{S} = i\alpha \ \text{diag}(\mathbf{R}, \mathbf{R}). \tag{C.3}$$

We note that the considered structure admits dispersive degeneracies such as Dirac cones when $\alpha = 0$, corresponding to the case of an ordinary hexagonal lattice without spinners, as shown in Fig. 25(a). The Dirac Point is at $K = (2\pi/3, 2\pi/(3\sqrt{3}))$ and $\omega = \sqrt{3/2}$ in the reciprocal lattice.

For $\alpha \to 1^-$, at the same point in the reciprocal space, another Dirac cone appears at a higher frequency. Such a case is shown in Fig. 25(b), for $\alpha = 0.999$. Actually, in this case the Dirac cone has not formed yet and an extremely narrow stop band is opened at the reciprocal point $K = (2\pi/3, 2\pi/(3\sqrt{3}))$, in the vicinity of the vertex of the Dirac cone appearing for $\alpha \to 1^-$.

Supplementary material

Supplementary material associated with this article can be found, in the online version, at https://doi.org/10.1016/j.ijengsci.2019.05.007.

References

Armanini, C., Dal Corso, F., Misseroni, D., & Bigoni, D. (2017). From the elastica compass to the elastica catapult: An essay on the mechanics of soft robot arm. *Proceedings of the Royal Society A: Mathematical, Physical and Engineering Sciences, 473*, 20160870.

Bacigalupo, A., & Gambarotta, L. (2016). Simplified modelling of chiral lattice materials with local resonators. *International Journal of Solids and Structures, 83*, 126–141.

Bigoni, D., Dal Corso, F., Misseroni, D., & Bosi, F. (2014). Torsional locomotion. *Proceedings of the Royal Society A: Mathematical, Physical and Engineering Sciences, 470*, 20140599.

Bordiga, G., Cabras, L., Bigoni, D., & Piccolroaz, A. (2018). Free and forced wave propagation in a Rayleigh-beam grid: Flat bands, Dirac cones, and vibration localization vs isotropization. *International Journal of Solids and Structures, 161*, 64–81.

Bosi, F., Misseroni, D., Dal Corso, F., & Bigoni, D. (2015). Self-encapsulation, or the 'dripping' of an elastic rod. *Proceedings of the Royal Society A: Mathematical, Physical and Engineering Sciences, 471*, 20150195.

Brun, M., Colquitt, D. J., Jones, I. S., Movchan, A. B., & Movchan, N. V. (2014). Transformation cloaking and radial approximations for flexural waves in elastic plates. *New Journal of Physics, 16*, 093020.

Brun, M., Giaccu, G. F., Movchan, A. B., & Slepyan, L. I. (2014). Transition wave in the collapse of the San Saba Bridge. *Frontiers in Materials, 1*, 12.

Brun, M., Guenneau, S., & Movchan, A. B. (2009). Achieving control of in-plane elastic waves. *Applied Physics Letters, 94*, 061903.

Brun, M., Jones, I. S., & Movchan, A. B. (2012). Vortex-type elastic structured media and dynamic shielding. *Proceedings of the Royal Society A: Mathematical, Physical and Engineering Sciences, 468*, 3027–3046.

Brun, M., Movchan, A. B., & Slepyan, L. I. (2013). Transition wave in a supported heavy beam. *Journal of the Mechanics and Physics of Solids, 61*(10), 2067–2085.

Cabras, L., Movchan, A. B., & Piccolroaz, A. (2017). Floquet-Bloch waves in periodic networks of the Rayleigh beams: Honeycomb systems, dispersion degeneracies and structured interfaces. *Mechanics of Solids, A Journal of Russian Academy of Sciences, 5*, 93–108.

Carta, G., Brun, M., Movchan, A. B., Movchan, N. V., & Jones, I. S. (2014). Dispersion properties of vortex-type monatomic lattices. *International Journal of Solids and Structures, 51*, 2213–2225.

Carta, G., Jones, I. S., Movchan, N. V., Movchan, A. B., & Nieves, M. J. (2017a). "Deflecting elastic prism" and unidirectional localisation for waves in chiral elastic systems. *Scientific Reports, 7*, 26.

Carta, G., Jones, I. S., Movchan, N. V., Movchan, A. B., & Nieves, M. J. (2017b). Gyro-elastic beams for the vibration reduction of long flexural systems. *Proceedings: Mathematical, Physical and Engineering Sciences, 473*, 20170136.

Carta, G., Nieves, M. J., Jones, I. S., Movchan, N. V., & Movchan, A. B. (2018). Elastic chiral waveguides with gyro-hinges. *The Quarterly Journal of Mechanics and Applied Mathematics, 71*, 157–185.

Cazzolli, A., & Dal Corso, F. (2019). Snapping of elastic strips with controlled ends. *International Journal of Solids and Structures, 162*, 285–303.

Chen, Z. G., & Wu, Y. (2016). Tunable topological phononic crystals. *Physical Review Applied, 5*, 054021.

Colquitt, D. J., Brun, M., Gei, M., Movchan, A. B., Movchan, N. V., & Jones, I. S. (2014). Transformation elastodynamics and cloaking for flexural waves. *Journal of the Mechanics and Physics of Solids, 72*, 131–143.

Dal Corso, F., Misseroni, D., Pugno, N. M., Movchan, A. B., Movchan, N. V., & Bigoni, D. (2017). Serpentine locomotion through elastic energy release. *Journal of the Royal Society Interface, 14*, 20170055.

Dehrouyeh-Semnani, A. M. (2015). The influence of size effect on flapwise vibration of rotating microbeams. *International Journal of Engineering Science, 94*, 150–163.

Dehrouyeh-Semnani, A. M., BehboodiJouybari, M., & Dehrouyeh, M. (2016). On size-dependent lead-lag vibration of rotating microcantilevers. *International Journal of Engineering Science, 101*, 50–63.

Del Vescovo, D., & Giorgio, I. (2014). Dynamic problems for metamaterials: Review of existing models and ideas for further research. *International Journal of Engineering Science, 80*, 153–172.

D'Eleuterio, G. M. T., & Hughes, P. C. (1984). Dynamics of gyroelastic continua. *Journal of Applied Mechanics, 51*, 415–422.

D'Eleuterio, G. M. T., & Hughes, P. C. (1987). Dynamics of gyroelastic spacecraft. *Journal of Guidance, 10*, 401–405.

Farhat, M., Guenneau, S., Enoch, S., & Movchan, A. B. (2009). Cloaking bending waves propagating in thin elastic plates. *Physical Review B, 79*, 033102.

Farokhi, H., Ghayesh, M. H., Gholipour, A., & Hussain, S. (2017). Motion characteristics of bilayered extensible Timoshenko microbeams. *International Journal of Engineering Science, 112*, 1–17.

Gao, W., Lawrence, M., Yang, B., Liu, F., Fang, F., Béri, J., et al. (2015). Topological photonic phase in chiral hyperbolic metamaterials. *Physical Review Letters, 114*, 037402.

Garau, M., Carta, G., Nieves, M. J., Jones, I. S., Movchan, N. V., & Movchan, A. B. (2018). Interfacial waveforms in chiral lattices with gyroscopic spinners. *Proceedings of the Royal Society A: Mathematical, Physical and Engineering Sciences, 474*, 20180132.

Ghayesh, M. H. (2018). Dynamics of functionally graded viscoelastic microbeams. *International Journal of Engineering Science, 124*, 115–131.

Ghayesh, M. H. (2019). Viscoelastic dynamics of axially FG microbeams. *International Journal of Engineering Science, 135*, 75–85.

Ghayesh, M. H., Farokhi, H., & Gholipour, A. (2017). Oscillations of functionally graded microbeams. *International Journal of Engineering Science, 110*, 35–53.

Goldstein, H., Poole, C., & Safko, J. (2001). *Classical Mechanics* (3rd ed.). Pearson.

Hassanpour, S., & Heppler, G. R. (2016a). Dynamics of 3D Timoshenko gyroelastic beams with large attitude changes for the gyros. *Acta Astronautica, 118*, 33–48.

Hassanpour, S., & Heppler, G. R. (2016b). Theory of micropolar gyroelastic continua. *Acta Mechanica, 227*, 1469–1491.

He, C., Chen, X. L., Lu, M. H., Li, X. F., Wan, W. W., Qian, X. S., et al. (2010). Left-handed and right-handed one-way edge modes in a gyromagnetic photonic crystal. *Journal of Applied Physics, 107*, 123117.

He, C., Ni, X., Ge, H., Sun, X. C., Chen, Y. B., Lu, M. H., et al. (2016). Acoustic topological insulator and robust one-way sound transport. *Nature Physics, 12*, 1124–1129.

Hughes, P. C. (1986). *Spacecraft attitude dynamics*. New York: Wiley.

Hughes, P. C., & D'Eleuterio, G. M. T. (1986). Modal parameter analysis of gyroelastic continua. *Journal of Applied Mechanics, 53*, 918–924.

Jin, D., Christensen, T., Soljačić, M., Fang, N. X., Lu, L., & Zhang, X. (2017). Infrared topological plasmons in graphene. *Physical Review Letters, 118*(245301), 1–6.

Khanikaev, A. B., Fluery, R., Mousavi, S. H., & Alú, A. (2015). Topologically robust sound propagation in an angular-momentum-biased graphene like resonator lattice. *Nature Communications, 6*, 8260.

Khanikaev, A. B., Mousavi, S. H., Tse, W. K., Kargarian, M., MacDonald, A. H., & Shvets, G. (2013). Photonic topological insulators. *Nature Materials, 12*, 233–239.

Kirillov, O. N. (2009). Campbell diagrams of weakly anisotropic flexible rotors. *Proceedings of the Royal Society A: Mathematical, Physical and Engineering Sciences, 465*(2109), 2703–2723.

Kirillov, O. N. (2013). *Nonconservative Stability Problems of Modern Physics*. Berlin, Boston: De Gruyter.

Kochmann, D., & Bertoldi, K. (2017). Exploiting microstructural instabilities in solids and structures: From metamaterials to structural transitions. *Applied Mechanics Reviews, 69*, 050801.

Lepidi, M., & Bacigalupo, A. (2018). Multi-parametric sensitivity analysis of the band structure for tetrachiral acoustic metamaterials. *International Journal of Solids and Structures, 136–137*, 186–202.

Makwana, M. P., & Craster, R. V. (2018a). Designing multidirectional energy splitters and topological valley supernetworks. *Physical Review B, 98*, 235125.

Makwana, M. P., & Craster, R. V. (2018b). Geometrically navigating topological platonic modes around gentle and sharp bends. *Physical Review B, 98*, 184105.

Milton, G. W., Briane, M., & Willis, J. R. (2006). On cloaking for elasticity and physical equations with a transformation invariant form. *New Journal of Physics, 8*, 248.

Misseroni, D., Colquitt, D. J., Movchan, A. B., Movchan, N. V., & Jones, I. S. (2016). Cymatics for the cloaking of flexural vibrations in a structured plate. *Scientific Reports, 6*, 23929.

Ni, X., He, C., Sun, X. C., Liu, X. P., Lu, M. H., Feng, L., et al. (2015). Topologically protected one-way edge mode in networks of acoustic resonators with circulating air flow. *New Journal of Physics, 17*, 053016.

Nieves, M. J., Carta, G., Jones, I. S., Movchan, A. B., & Movchan, N. V. (2018). Vibrations and elastic waves in chiral multi-structures. *Journal of the Mechanics and Physics of Solids, 121*, 387–408.

Nieves, M. J., Mishuris, G. S., & Slepyan, L. I. (2016). Analysis of dynamic damage propagation in discrete beam structures. *International Journal of Solids and Structures, 97–98*, 699–713.

Nieves, M. J., Mishuris, G. S., & Slepyan, L. I. (2017). Transient wave in a transformable periodic flexural structure. *International Journal of Solids and Structures, 112*, 185–208.

Norris, A. N. (2008). Acoustic cloaking theory. *Proceedings of the Royal Society A: Mathematical, Physical and Engineering Sciences, 464*, 2411–2434.

Norris, A. N., & Shuvalov, A. L. (2011). Elastic cloaking theory. *Wave Motion, 48*, 525–538.

Padovan, J. (1978). On gyroscopic problems in elasticity. *International Journal of Engineering Science, 16*, 1061–1073.

Padovan, J. (1979). Gyroscopic effects in micropolar elasticity. *International Journal of Engineering Science, 17*, 433–439.

Padovan, J., & Adams, M. (1980). On nonconservative gyroscopic eigenvalue problems in elasticity. *International Journal of Engineering Science, 18*, 1333–1348.

Pal, R. K., & Ruzzene, M. (2017). Edge waves in plates with resonators: an elastic analogue of the quantum valley Hall effect. *New Journal of Physics, 19*, 025001.

Parnell, W. J. (2012). Nonlinear pre-stress for cloaking from antiplane elastic waves. *Proceedings of the Royal Society A: Mathematical, Physical and Engineering Sciences, 468*, 563–580.

Piccolroaz, A., Movchan, A. B., & Cabras, L. (2017a). Dispersion degeneracies and standing modes in flexural waves supported by Rayleigh beam structures. *International Journal of Solids and Structures, 109*, 152–165.

Piccolroaz, A., Movchan, A. B., & Cabras, L. (2017b). Rotational inertia interface in a dynamic lattice of flexural beams. *International Journal of Solids and Structures, 112*, 43–53.

Rafsanjani, A., Zhang, Y., Liu, B., Rubinstein, S. M., & Bertoldi, K. (2018). Kirigami skins make a simple soft actuator crawl. *Science Robotics, 3*(15), eaar7555.

Raghu, S., & Haldane, F. D. M. (2008). Analogs of quantum-Hall-effect edge states in photonic crystals. *Physical Review A, 78*, 033834.

Shafiei, N., Kazemi, M., & Ghadiri, M. (2016). On size dependent vibration of rotary axially functionally graded microbeam. *International Journal of Engineering Science, 101*, 29–44.

Souslov, A., van Zuiden, B. C., Bartolo, D., & Vitelli, V. (2017). Topological sound in active-liquid metamaterials. *Nature Physics, 13*, 1091–1094.

Süsstrunk, R., & Huber, S. D. (2015). Observation of phononic helical edge states in a mechanical topological insulator. *Science, 349*(6243), 47–50.

Wang, P., Lu, L., & Bertoldi, K. (2015). Topological phononic crystals with one-way elastic edge waves. *Physical Review Letters, 115*, 104302.

Wang, Z., Chong, Y. D., Joannopoulos, J. D., & Soljačić, M. (2008). Reflection-free one-way edge modes in a gyromagnetic photonic crystal. *Physical Review Letters, 100*, 013905.

Yamanaka, K., Heppler, G. R., & Huseyin, K. (1996). Stability of gyroelastic beams. *AIAA Journal, 34*, 1270–1278.

Yang, Z., Gao, F., Shi, X., Lin, X., Gao, Z., Chong, Y., & Zhang, B. (2015). Topological acoustics. *Physical Review Letters, 114*, 114301.

Zheng, L. Y., Teocharis, G., Tournat, V., & Gusev, V. (2018). Quasitopological rotational waves in mechanical granular graphene. *Physical Review B, 97*, 060101(R).

Zhou, X. M., & Zhao, Y. C. (2019). Unusual one-way edge state in acoustic gyroscopic continuum. *Science China Physics, Mechanics and Astronomy, 62*, 014612.